FACET PHASE EFFECTS IN DFB DIODE LASERS

FACET PHASE EFFECTS IN DFB DIODE LASERS

By

JAY WELBOURN, B.Sc.

A Thesis
Submitted to the School of Graduate Studies
in Partial Fulfilment of the Requirements
for the Degree
Master of Applied Science

McMaster University

MASTER OF APPLIED SCIENCE (2003) McMaster University
Department of Engineering Physics Hamilton, Ontario

TITLE: Facet Phase Effects in DFB Diode Lasers

AUTHOR: Jay Welbourn, B.Sc. (University of Guelph)

SUPERVISOR: Dr. Daniel T. Cassidy

NUMBER OF PAGES: ix, 78

Abstract

A transfer matrix model of distributed feedback (DFB) lasers was fit to experimental laser spectra, thereby extracting physical laser parameters. This was done in order to monitor facet degradation during aging studies of 11 DFB laser devices. Ten devices had no observable spectral changes, and one device had spectral changes that could be fitted to by varying the model's front facet phase and reflectivity parameters. Comparison of this result with measurements of degree-of-polarization (DOP) photoluminescence maps of the laser facet showed a unique stress pattern on the facet that could possibly indicate changes in facet properties.

The effective linewidth enhancement factor (LEF) and frequency response were measured from four devices to determine if spatial holeburning affects the dynamic behaviour of DFB lasers enough to cause performance differences between devices. No obvious differences between frequency responses of the four devices were observed, and LEF values of 5-6.5 were extracted from the response data. Comments on the validity of the LEF calculation are made.

Acknowledgements

I'd like to thank my supervisor Dr. Daniel Cassidy for supporting this study, and for sharing his wisdom and research skills with me.

Robert Mallard, Kenton White and Greg Letal at Bookham Technologies provided the devices for study, performed the aging of the devices, and were always available to answer my questions.

Doug Bruce was always there when I needed help designing experiments and obtaining equipment.

The lab mates that I have spent my time with have been invaluable contributors to my work and my sanity. Thank you to: Gord for providing excellent TMM code and helping me decipher and understand it; Sam for his aging expertise and performing PL measurements; Mark for discussing stress effects and providing software to display PL measurements; Aaron for helping me with the high speed measurements and theory; and Sean, Huiling and Jing Cong for frequent discussions and help with laser theory.

Finally, I thank my wife Samantha for her perpetual love, encouragement and support.

Contents

List of Tables

List of Figures

Chapter 1

Introduction

Distributed feedback (DFB) diode lasers are applied widely as narrow linewidth coherent light sources. Manufacturing and design techniques have been refined to a level such that operating characteristics of such lasers can be controlled to high precision and the lasers are reliable with long lifetimes. With modern semiconductor growth and processing techniques, most aspects of design can be controlled within design tolerances; however, the location of the cleaved surface of the laser along the laser cavity can only be controlled within a precision of a few microns. This uncertainty is larger than the grating period length of the laser, and results in the cleaved surface being positioned at a random position along the grating period. This position is called the facet phase, defined in degrees with respect to one grating period. The facet phase parameter affects the shape of the laser spectrum, and the spatial holeburning (SHB) distribution in the laser cavity. This study was done in two parts to attempt to monitor such facet effects in DFB lasers.

The first part of the study examined how aging DFB lasers affected their below threshold spectra. The dependance of DFB spectra on facet phase and reflectivity makes the below threshold spectrum an appropriate measurement to monitor possible changes in facet parameters. The laser facet was also monitored by photoluminescence (PL) mapping of the facet surface. The results from these two monitoring techniques were compared.

The second part of the study examined the effect of facet phase on the frequency modulated (FM) response and effective linewidth enhancement factor (LEF) of DFB laser diodes. The SHB distribution of a DFB laser diode is dependant on the facet phase of the device, and affects the shape of the spectrum of the device by modifying the characteristics of the laser waveguide. This implies that the SHB distribution also affects the FM response and the effective LEF of the device. To test this idea, the FM response was measured from four devices of the same batch, and effective LEF values were extracted from these measurements. Differences in results between the devices may be caused by facet phase effects on the SHB distribution in the devices.

This report is divided into four chapters. This chapter offers a brief overview of the study. Chapter 2 provides an introduction to the transfer matrix model that is used to extract physical laser parameters from experimental spectra, and how the parameters affect a laser spectrum. Chapter 3 describes the aging experiment that was performed, presents results from the experiment and discusses the results.

Chapter 4 describes the experiment that measured the FM response and effective LEF of four lasers, presents results from the experiment and discusses the results. Concluding remarks are made in Chapter 5 along with suggestions for further study opportunities. References cited in this report are listed following Chapter 5 in the Bibliography.

Chapter 2

Transfer Matrix Model of DFB Lasers

2.1 DFB Theory

In simple Fabry-Perot lasers, the feedback necessary for laser oscillation is provided by means of reflection at the two end facets of the laser cavity. The effect of this feedback has a periodic wavelength dependance due to the interference of the reflected light with the incident light. In a passive medium, such feedback creates the well known Fabry-Perot (FP) transmission fringe pattern:

$$|T| = (1 + F_1 \sin^2(\delta/2))^{-1}, \tag{2.1}$$

with $\delta = 2k_o n_e L \cos(\theta)$ the optical phase acquired through one round trip through the laser, and $F_1 = 4R/(1-R)^2$ is the coefficient of finesse, which determines the transmitted flux-density distribution (how sharp the transmission peaks are).

When a FP cavity contains a gain material, as in a laser, the output light intensity is described by an expression that contains elements of the FP transmission function:

$$I \propto \frac{1+RG}{(1-RG)^2 \cdot (1+F_2 \sin^2(\delta/2))}, \tag{2.2}$$

with G the single pass intensity gain of the medium, δ as defined above, and $F_2 = 4RG/(1-RG)^2$ is the modified coefficient of finesse. Because of the periodic nature of the FP transmission function, with the Free Spectra Range (FSR) smaller than the gain width of semiconductor materials, Fabry Perot lasers suffer from multimode operation at low operating powers, mode hopping with changes in current and temperature, and low side mode suppression ratios at high operating powers.

DFB lasers employ a similar basic design to the FP laser, but in addition to the two facet reflections, they incorporate a Bragg grating in their guiding region to provide a feedback mechanism that is distributed throughout the laser cavity. A Bragg grating is a waveguide having a longitudinally varying index of alternating high and low index sections.. This distributed feedback affects wavelengths that are close to half-integer multiples of the Bragg period, and since gain curves only span a limited bandwidth, DFB lasers are usually designed to operate only on the first order of the Bragg grating. Therefore, although the Bragg feedback also has a periodic effect with wavelength, only one section of its period overlaps the laser emission spectrum and so the laser spectrum is only affected by one period of the Bragg reflection spectra. This characteristic of DFB lasers accounts for the single mode operation, high SMSR, and narrow linewidth that makes these lasers so useful.

Spectra of lasers that incorporate a Bragg reflector can be described in many ways, including the coupled mode theory and the transfer matrix method.

2.1.1 Coupled Mode Theory

Coupled mode theory is an approximate theory that is based upon perturbation analysis of the waveguide. It is limited by requiring a small, sinusoidal index perturbation, and is difficult to adapt to include longitudinally varying material parameters (1). Coupled mode theory has been widely applied to calculate DFB spectra quickly using boundary conditions to include facet effects; however, it has been shown that it is not accurate for certain applications (2).

Coupled-mode theory can be used for demonstration purposes due to the simplicity of its analytical expressions. From coupled-mode theory, the power reflection spectrum of a Bragg grating can be expressed as (3):

$$R = \frac{\sinh^2(\sqrt{\kappa^2 - \sigma^2}L)}{\cosh^2(\sqrt{\kappa^2 - \sigma^2}L) - \frac{\sigma^2}{\kappa^2}} \tag{2.3}$$

where $\kappa = \frac{\pi}{\lambda}\Delta n_e$ is the coupling coefficient induced by the index grating, and $\sigma = \beta - \pi/\Lambda = 2\pi n_e(\frac{1}{\lambda} - \frac{1}{\lambda_B})$ is the detuning parameter that accounts for the deviation of the wavelength of interest (λ) from the Bragg wavelength ($\lambda_B = 2n_e\Lambda$ with Λ the period of the Bragg grating). This reflection spectra expression is plotted in Fig. 2.1 for a range of κL values. The high reflection regions of the reflection spectra have increased scattering losses in a DFB cavity, and this increased scattering creates the

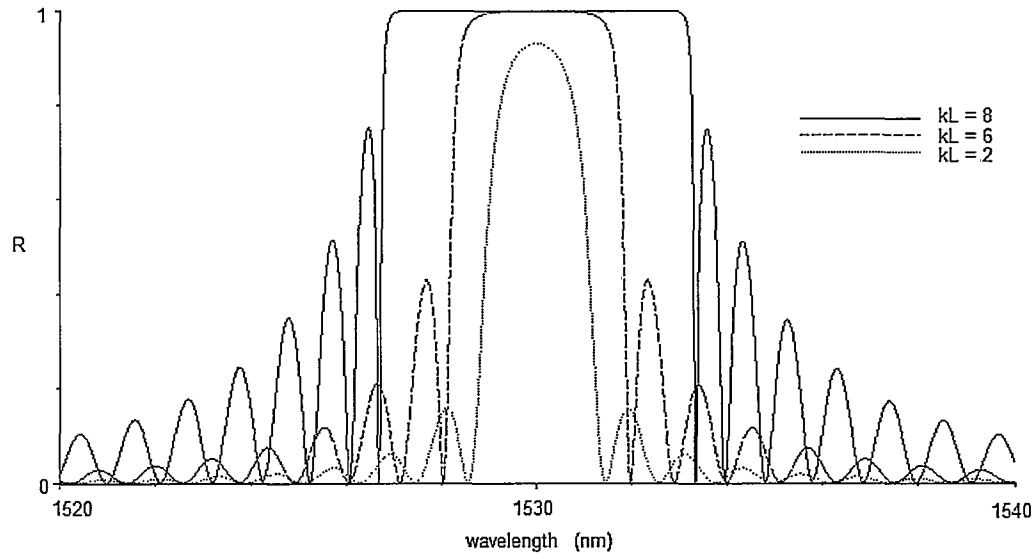

Figure 2.1: Bragg grating power reflection spectra near Bragg wavelength of 1530 nm

stopband section of a DFB spectra. Notice that the influence of the grating drops off as wavelengths move away from the Bragg wavelength. To complete the calculation of a DFB laser spectra, knowledge of the gain properties of the active region and the influence of facet reflections on the round trip phase condition in the cavity are necessary.

The transfer matrix method is an alternative method to calculate the spectra of devices that employ Bragg gratings. It assumes square wave perturbations of the effective index of the waveguide, isn't limited to small index perturbations, and can easily include longitudinally varying material parameters. This allows the transfer matrix method to model longitudinal variations in carrier and photon densities that

affect DFB lasers.

The TMM also is well suited for truncated well lasers, where the active region of the laser is included in the index perturbation, creating a complex coupling coefficient. In such lasers, the resonant standing wave effect must be accounted for. This effect preferentially amplifies the long wavelength Bragg mode over the short wavelength Bragg mode, and is a result of the intensity distribution of the long wavelength Bragg mode overlapping the high index, high gain sections of the grating more than the intensity distribution of the short wavelength Bragg mode. The intensity distribution of the short wavelength Bragg mode has a larger overlap with the low index, low gain sections of the grating. The resonant standing wave effect is accounted for in the TMM model (4)(5).

2.1.2 Transfer Matrix Method

The transfer matrix method is a one dimensional approach that divides the laser cavity into a series of homogeneous sections, each of which represents one of two sections that make up a period of the Bragg grating (6). Light propagation along the laser cavity can then be modelled by the multiplication of alternating propagation and interface matrices, with propagation occurring through one homogeneous section and the interface representing the boundary between the index of one section and the index of the neighboring section. The transfer matrix method easily includes subtle effects in DFB lasers, such as arbitrary facet phases and non-uniform gratings, by

appropriate adjustment of these transfer matrices.

If a longitudinally uniform grating exists (as can be assumed in below threshold laser cavities), mathematical simplifications can be employed to make the TMM an efficient method of calculating below threshold spectra (2). If the grating is non-uniform (as occurs when the non-uniform intensity distribution in the laser cavity gives rise to a non-uniform carrier distribution, affecting the uniformity of the gain and index through the differential index and gain of the material), then the TMM can accurately include the changes as well (5).

The TMM used in this work was developed previously (2), and modified slightly for efficient application to this study. This model worked in two modes of operation: a below threshold model that employs a Marquardt least-squares fitting algorithm to fit laser parameters to below threshold laser spectra (7)(8), and an above threshold model that accurately calculates intensity distributions along the laser cavity and uses a standard rate equation to find the steady-state carrier distribution along the laser cavity (4)(5).

2.1.2.1 Limitations of This TMM

The transfer matrix method is limited in its accuracy only by the level of detail that the programmer wishes to include. For the purposes of this study, a few obvious limitations were not corrected for. These limitations are listed below along with justification for not correcting them:

1) The grating is assumed to be uniform below threshold. This uniformity includes the grating period and depth, and the waveguide's effective index.

This is an appropriate assumption, since grating manufacturing generally successfully attempts to make the grating as uniform as possible, so any deviation from this uniformity would be unexpected and difficult to predict accurately.

2) The reflectivities of the facets are assumed to be independent of wavelength. This assumption is obviously not adequate far from the stopband; however, the effects of wavelength dependant facet reflectivity can be approximated by adjusting the shapes of the gain curves appropriately. It would be beneficial to employ a rigorous model of facet coatings to model wide-band DFB spectra more accurately using facet coating design theory. This is a sophisticated field that requires consideration of Maxwell's equations for a three-dimensional boundary value problem (9). Such an approach should properly account for the elliptical diffraction that a beam undergoes while propagating through the coating. Attempting to model facet coatings to this accuracy is beyond the requirements of this study since the gain curve adjustments that we apply are able to expose the spectral changes that we are interested in observing.

3) The material gain spectrum is approximated by modified parabolic expressions, and the spontaneous emission spectra is also represented by an appropriate expression. These approximations are reasonable for quantum well devices (2), and the benefits

of calculating the gain curves accurately through band modelling are not significant since the necessary parameters used to calculate these curves may not be readily available to the user of this model.

4) Differential index and gain are approximated to be constants since under small signal modulation, refractive index can be approximated as varying linearly with carrier density due to the plasma effect. (10)

2.2 Qualitative Effects of Model Parameters

Fitting calculated spectra to experimental spectra requires a good estimation of parameters for the automated least-squares routine to start from, otherwise the routine can find itself locked in an unphysical local χ^2 minimum. Human estimation requires an understanding of the effects that different model parameters have on the spectrum. These effects are summarized below.

- **Effective index (n_e), grating period (Λ)** These two parameters act together to determine the position of the Bragg stopband, according to the Bragg wavelength value $\lambda_{bragg} = 2n_e\Lambda$.

- **Index step of grating (Δn_e)** The index step determines the strength of the distributed feedback in the laser cavity. A higher Δn_e value increases the distributed feedback contribution to the spectra. Higher feedback manifests itself in a wider stopband and distributed feedback effects over a wider bandwidth

from the stopband, as seen in Fig. 2.1.

- **Number of grating periods** The number of grating periods determines the length of the laser cavity ($\#periods \times \Lambda = L$). The length of the cavity determines the Fabry-Perot fringe spacing (Free Spectral Range, or FSR) through the relationship $\Delta\lambda_{FSR} = \lambda^2/2n_gL$.

  The cavity length also affects the amount of distributed feedback the laser experiences through the coupled mode theory parameter $\kappa L = \frac{\pi}{\lambda}\Delta n_e L$.

- **Gain/spontaneous emission curves** The gain and spontaneous emission curves set the shape of the laser spectra. If the laser is a gain-coupled DFB laser (the grating perturbs both real and imaginary indices), then the curves will be different for the high and low index sections of the grating. As mentioned in Section 2.1, high and low index sections of the grating affect different wavelength sections of the spectrum differently due to the standing-wave resonance effect.

- **Facet phase** (ϕ_f, ϕ_b)

  Laser facet cleaving is done within an accuracy on the order of 10^{-5} m, while the period of the grating is on the order of 2×10^{-7} m. The result of this difference is that the exact position of the cleaved facet in the grating period (the facet phase) is random, and so the facet phase cannot be controlled during cleaving.

As explored in (7)(8), the phase of the facet affects the spectra in many ways, including:

- The wavelength position of flattened modes;
- The wavelength position of FP modes;
- Ramping effects;
- The wavelength position of possible stopband modes; and,
- The relative amplitude of long and short wavelength Bragg modes.

The lasers studied in this report employ a high reflectivity (HR) coating on one facet, and an anti-reflective (AR) coating on the other, which makes isolation of facet phase effects simpler. The HR coated facet contributes a significant amount to the spectrum near the Bragg wavelength due to the high level of feedback coming from that facet. Small changes in this facet phase are easily seen in the spectrum near the stopband, and this sensitivity allows the phase of this facet to be determined by fitting over this wavelength range. The AR coated facet contributes a far lesser amount to the spectrum near the Bragg wavelength due to the low level of feedback coming from that facet. This facet phase modifies the FSR through its effect on the total length of the laser. By modifying the FSR of the laser, the AR coated facet phase changes the wavelength positions of the Fabry-Perot fringes.

- **Facet reflectivity** (R_f, R_b)

  The reflectivity of the individual facets determines how strongly the phase of the facet will affect the spectrum. The phase of AR coated facets has little effect on the DFB portions of the spectrum near the stopband, while the phase of HR coated facets has a larger effect on these portions of the spectrum.

  Since the facet reflections work together to form the interference that creates Fabry-Perot modes, the reflectance of both facets $(R_f \times R_b)$ determines the amplitude of the Fabry-Perot envelope. This amplitude is also affected by the material gain of the laser as was shown in Eq. 2.2.

Chapter 3

Monitoring Spectra during Aging of Lasers

3.1 Reliability and Accelerated Life Testing

The reliability of semiconductor lasers is an important aspect of device research and design. Understanding degradation mechanisms that are involved during device aging allows engineers to design devices that are reliable with mean lifetimes of >500,000 hours (11). Device lifetimes of this duration are necessary for many applications, such as trans-Atlantic long haul communication systems.

Reliability of a device refers to the ability of a device to operate within a defined environment over a certain period of time (11) and as such, any number of factors can affect the reliability of a device depending on what environment the device is set to operate under.

Device failure generally occurs at a rate that follows a "bathtub" curve, whereby failures occur early during operation at a decreasing rate that approaches a steady

state. This steady state is maintained until the failure rate increases again late in the devices' operation. This curve can be derived from the Weibull distribution. This distribution defines the failure distribution function (the fraction of devices that have failed up to a given time) as:

$$1 - exp\{-[(t-\gamma)/\eta]^m\}, \tag{3.1}$$

with m determining if the failure rate is decreasing ($m < 1$), constant ($m = 1$) or increasing ($m > 1$), η determining the rate of changing failure rate, and γ determining the position of the curve with time. Early failure is represented by the region where $m < 1$, the steady state region is represented when $m = 1$, and late failure is represented by the region where $m > 1$.

The Weibull distribution function results in the following expression for the failure rate:

$$(m/\eta)[(t-\gamma)/\eta]^{m-1}. \tag{3.2}$$

This expression is the mathematical expression for the "bathtub" curve described above.

By employing a burn-in test during device screening, devices that fail during the early period are discarded and subsequent device failure is limited to steady state or late failures. Devices are designed to operate in the steady state regime of the failure rate curve for the duration of the device's lifetime, and so device failure is generally

caused by slow, deterministic degradation mechanisms that are characteristic of the steady state regime.

Most deterministic degradation mechanisms are assumed to be the result of a specific reaction (diffusion, precipitation, oxidation, etc.) occurring in a material that over time alters the device's operating characteristics by an unacceptable level. These reactions usually have a threshold activation energy, E_a, associated to them which must be overcome before the reaction will proceed. Since the energy distribution of particles (atoms) in a material follows the Boltzmann distribution $P(E) = exp(-E/kT)$, it follows that the rate of degradation will be proportional to the number of particles that have the necessary energies to activate the degradation mechanism. This idea is summarized in the Arrhenious relation: $lifetime = A_T \cdot exp(E_a/kT)$, and is the basis of the theory of temperature accelerated aging.

Temperature accelerated aging operates the device under test (DUT) in an environment of elevated temperature to increase the number of particles that can overcome a particular activation energy, thus accelerating the rate of degradation. This allows the DUT's reliability performance to be simulated over timescales that would otherwise be impractical.

3.2 Aging Effects in InGaAsP Lasers

Degradation mechanisms in semiconductor lasers can be categorized into those originating from material properties (defects, etc.), and those originating from device packaging (bonding stresses, etc.).

3.2.1 Material Effects

Device degradation can be caused by properties of the semiconductor materials used in the device. If the material is of poor quality, dark defects (precipitation of host atoms cause defects that appear as dark spots in electro-luminescence scans) or crystal dislocations can appear. These defects change the binding state between electron and atom, causing non-radiative recombination in the device, and raising the threshold current of the device.

The surface of a device, where the material is in contact with the surrounding environment, consists of many dangling bonds and can have a higher concentration of impurities because of this. These factors cause non-radiative recombination, heating and degradation of the device.

Also dependant on material properties of the device is degradation of the facet. Facet degradation can be gradual, whereby a photo-assisted reaction oxidizes the active region material at the surface, or sudden as in catastrophic optical damage

(COD). Facet oxidation causes non-uniform film growth, and so its effect is a scattering of output light rather than a change of facet reflectivity. COD is a sudden degradation that melts the facet when light output exceeds a certain level, and it is caused by the absorption of emitted light at the facet.

3.2.2 Device Packaging Effects

The packaging of a device can affect the reliability of a device's inner region, or it can degrade directly and cause device failure.

Metal diffusion from p-side electrodes along the direction of current flow into the active region of a device can cause dark defects and, subsequently, non-radiative recombination.

The solder used to bond a chip to its carrier can migrate during aging, causing whisker growth over the facet, and even shorting out the device if growth is extensive. The solder itself can also fail, from thermal fatigue or void formation at the bond.

The bonding agent induces stresses in devices, caused by a difference in the thermal expansion coefficients between the carrier, bonding agent, and chip material. Since bonding occurs at elevated temperatures, the cooling of the device to operating temperature from bonding temperature induces stresses in the device. Aging of devices often changes the stress patterns through stress relaxation.

3.2.3 Effects Relevant to InGaAsP Devices

InGaAsP laser diodes are very stable during aging and consequently have long lifetimes. This feature of the devices can be attributed to the stability of InGaAsP material when exposed to air, high quality wafers that minimize material defects, the high resistance of InGaAsP to degradation enhanced by non-radiative recombination, and the high level of catastrophic optical damage in InGaAsP that is not easily attainable during operation.

These features of InGaAsP result in devices made of the material having fewer material based reliability problems than GaN based devices. InGaAsP devices' failure mechanisms are limited mostly to degradation of device packaging. This degradation can be controlled by careful selection of bonding and soldering agents.

Due to these reasons, we do not expect to observe material based reliability problems or device packaging degradation in this study. Of primary concern to this study is the aging of facet coatings.

3.2.4 Previous work with Aging of Facet Coatings

Photoluminescence (PL) monitoring during aging (12) has shown changes in PL temporal responses and intensity that may indicate effusion of hydrogen from the silicon film coatings of the devices. One influence of hydrogen on amorphous silicon is to lower the index of refraction (13), and it would be assumed that such a change in

index with aging would affect the performance of a thin film coating. It has not yet been determined if these changes that are observed through PL measurements can be observed as changes in the below threshold spectra of the lasers.

3.3 Coating Theory

Optical interference coatings are commonly applied to the facets of diode lasers to improve the operating characteristics and versatility of the devices (9). High Reflectivity (HR) coatings are employed to increase the feedback of light within the cavity, and Anti-Reflectivity (AR) coatings are used to allow light to preferentially exit from one facet (the front facet) of the laser.

Optical coatings are created by the deposition of thin film layers on a substrate, and act through optical interference (14). To model an optical coating, the system consisting of the substrate and thin film layers can be represented by the optical admittance which is the ratio of the magnetic and electric field of the EM wave through the system (9). AR coatings are designed to match this admittance to that of the ambient medium, while HR coatings are designed to contrast the two admittances.

Coating design involves balancing the reflectance level, the width of the reflectance band, and design simplicity. These factors are dependant upon the effective thickness of the layers, uniformity of the layers, and the number of interference layers. When

any of these parameters are changed, the performance of the coating is affected, thereby affecting the performance of the device using the coating.

The work performed for this study sought to determine if possible changes in coatings during aging of the devices could be correlated to possible changes in laser spectra.

3.4 Facet Effects on DFB Spectra

The spectra of DFB lasers are highly dependant on the condition of the two end facets of the laser. The facets are created when the laser bar is cleaved to its desired length during processing, and the reflectivity of those facets is modified from the as-cleaved reflectivity when facet coatings are applied. The facet phase and reflectivity can be determined by fitting below threshold spectra to a transfer matrix model of the laser spectra that includes these parameters. This is possible because each facet parameter affects the laser spectra differently, as discussed in Section 2.2.

3.5 Experimental Details

3.5.1 Spectral Measurements

Spectral measurements of the devices were taken by mounting the devices on a copper block that was temperature controlled to room temperature with stability of $\pm 0.1\,^{\circ}\mathrm{C}$ using a McMaster analogue PID controller. The lasers were then current driven by a McMaster laser driver over a range of below threshold bias levels.

Collection of the output light was done in two ways, the first to determine the spectra with minimal back-reflection into the laser cavity, and the second to provide a measuring procedure that allowed a large number of measurements to be made in a reasonable amount of time.

In the first procedure, the laser output was collected with a 1" F1 plano-convex lens, sent through a Faraday optical isolator (Optics for Research) and focused with a second 1" F1 plano-convex lens into a single mode fibre patch cable mounted on a 3 axis piezo-actuated stage. The combination of plano-convex lenses and the optical isolator rotated at a slight angle of $\sim 5\,^{\circ}$ from the optical axis minimized any possible back reflections into the laser cavity. A schematic of this setup is shown in Fig. 3.1

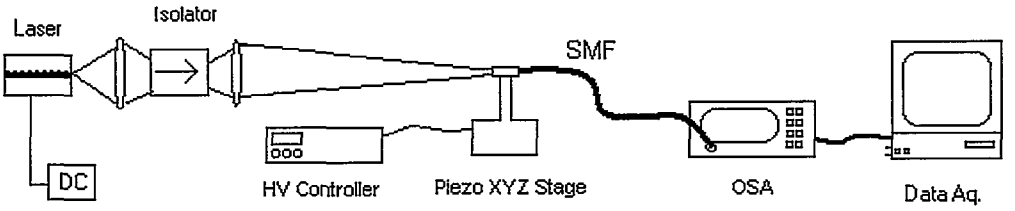

Figure 3.1: Setup for open air coupling of laser output into single mode fibre.

The second procedure took less time to align than the open air fibre coupling of the first procedure. This technique employed a tapered fibre to collect the laser output instead of the lens system described above. This fibre was mounted on a 4 axis piezo-actuated stage, and brought to within a few microns of the laser facet. The effect of back reflections on the laser spectra was evident as a long period oscillation

of the FP envelope when the fibre was brought too close to the laser facet. By comparing the spectra taken from this second procedure to the spectra taken from the first procedure, and adjusting the fibre position from the laser facet, the effects of back reflection from the fibre tip on the laser spectra were avoided.

The optical fibre was connected to an Optical Spectrum Analyzer (Anritsu MS9710C), which recorded the spectra to a high resolution and accuracy (wavelength resolution of 0.05 nm $\pm$ 2.2 %, accuracy of $\pm$ 200 pm, level accuracy of $\pm$ 0.4 dB and stability of $\pm$ 0.02 dB) (15). Spectra was taken over a wavelength range of 72 nm to ensure FP modes could be fitted to the model over a wide bandwidth.

3.5.1.1 Spectral Fitting Details

Spectral fits were performed on spectra to determine if facet changes were occurring during the aging process. Five sets of spectral data were taken to monitor when any spectral changes occurred, to ensure that the spectra were stable when taken under similar conditions, and to ensure that the procedure itself didn't affect spectral measurements. The chips were initially bonded to a carrier before the study commenced, and this carrier was later bonded to a submount for aging. The five data sets are as follows:

1. Original Set: Measured using the open-air light coupling procedure to determine initial spectra with minimal back-reflections.

2. Post PL Set: Measured after initial PL measurements to observe the effect of PL measurement process on spectra.

3. Post Bond Set: Measured after the carriers were bonded to aging submounts to observe the effect of this bonding on spectra. Note that this bonding is not expected to affect the the bonding stresses associated with bonding the laser chip to its carrier (16), and so effects on the spectra are not expected to be significant for this secondary bonding.

4. Post Burn-in Set: Measured after the initial 24 hours of aging under 100 °C and 150 mA conditions. The burn-in was performed to determine if any devices had early failure, as described in Section 3.1.

5. Post Aging Set: Measured after 900 hours of aging under 100 °C temperature and 150 mA bias level. Previous work with aging of coatings shows that the reverse burn-in phenomena should be saturated by this time (12).

The first data set was used to determine of the initial laser parameters, many of which are not expected to change over the course of the study.

Each subsequent data set was fitted using the parameters found from the first data set, allowing only the gain/spontaneous emission amplitudes and the effective index of the laser to vary during fitting. These parameters compensate for the variation of current and temperature between data sets that are necessary to obtain similar

spectra of devices that are undergoing changes in their threshold currents.

By fitting in this manner, any spectral changes that cannot be fitted to are highlighted and further investigated as possible symptoms of physical laser changes.

3.5.1.2 Spectral Fitting Procedure

Through the course of this study, an approach was found that allows a systematic determination of fitting parameters. This approach determines fitting parameters in a logical order which allows the parameter set to converge efficiently towards an accurate fit.

1. n_e: Set effective index to 3.2. This is a reasonable estimate of the index of InGaAsP at these wavelengths (17), and the accuracy of the value is not essential since the parameter is always used in combination with uncertain lengths in calculating effective path lengths.

2. Λ: Find the grating period that aligns the stopband wavelength of the fit with that of the data.

3. Δn_e: Find an approximate index step to make the stopband width of the fit approximately equal to that of the data. Note that facet phase can also affect the stopband width, so this value is approximate at this point.

4. L: Adjust the number of grating periods (thereby changing L) to make the Fabry-Perot fringe spacing equal to that of the data.

5. **Gain Parameters**: Estimate the gain peak wavelength and gain curve widths from the shape of the spectrum taken over a large bandwidth.

   The gain peak amplitudes and spontaneous emission rates are more difficult to estimate, making the use of the fitting routine useful for this task.

   The gain peak amplitudes of high and low index sections affect which sideband reaches threshold first, while the averaged gain peak amplitudes affect the relative amplitude of the lasing peak and its side modes. The high index gain preferentially acts upon the long wavelength sidebands and the low index gain preferentially acts upon the short wavelength sidebands through the standing wave effect (5).

   A routine was added to the fitting program that determined the envelope function of the FP modes of the data and the fit. Using this envelope function to fit the gain curves allows the gain widths and peak values to be found without requiring alignment of FP modes. This is helpful because, owing to the nature of least-squares fitting, the FP mode structure sometimes makes an unphysical least-squares fit more favourable to a more physical fit having a slightly higher χ^2 value.

6. **Facet Reflectivities**, R_f, R_b: Assuming the coatings are of known types, first estimate the reflectivities appropriately, and adjust to fit the amplitude of the

Fabry-Perot fringes and the shape of the spectra near the stopband. These parameters must be chosen with consideration of gain levels, as the FP fringe amplitudes result from the term $R_f \cdot R_b \cdot G$ in Eq. 2.2.

7. **Facet Phases,** ϕ_f, ϕ_b: Assuming the laser has HR and AR coated facets, first fit the HR coated facet to obtain spectra that are similar to the data near the stopband. The envelope function routine is useful for fitting this parameter; however, since the spectrum is affected in so many unpredictable ways by the facet phase, an additional routine was added to help find this parameter. This routine scans through a range of facet phases, calculating and storing the spectrum at each phase value. This allows the user to later view quickly the effect that facet phase has on devices' spectra to choose an approximate value for the phase.

   Once the HR coated facet phase has been determined, the AR coated facet phase can be determined by aligning the FP mode peaks far from the stopband. A change of 180° of the facet phase will shift the FP peaks by $\lambda_{FSR}/2$. Note that subsequent fine-tune changes in the HR coated facet phase will require an equivalent shift in the AR coated facet phase to maintain this FP peak alignment.

8. n_g: Group index controls the wavelength dependance of the index. By adjusting

n_g, FP mode peaks can be aligned far from the stopband. Group index should be fitted along with ϕ_f to correctly align FP modes along the whole wavelength range of the spectra.

By following the above procedure, a reasonable starting estimate of the fitting parameters can be found quickly.

After the initial estimate has been determined, iterative manual fine tuning of the parameters and execution of the least-squares fitting routine is necessary to obtain accurate fits.

3.5.2 PL Measurements

The polarization-resolved photoluminescence measurement technique (18) can be used to measure material stresses in crystal material by comparing the emission intensities of the TE and TM polarized light from material that is pumped via an external laser source. This technique probes the device over the surface of the material, creating a 2-dimensional surface map of the material and therefore is useful for measuring laser facet properties.

In previous studies (12), aging of facet coatings has been observed as a reduction in the amount of 'reverse burning' that is evident during measurement of the PL map. Reverse burning is when the PL intensity increases as the time of measurement increases. As mentioned in Section 3.2.4, it is thought that this reduction of reverse

burning is evidence of the effusion of hydrogen from the thin film coatings of the devices, which would result in changes of facet properties through changes of the coating material properties.

One intent of this study is to determine if the changes observed through PL measurements can be correlated to changes in facet coatings by observing the below threshold spectra of the devices, and to determine if any such changes can be fitted to using the TMM laser model by adjusting facet fitting parameters appropriately.

3.5.3 Aging Details

The lasers were sent to Bookham Technologies to be aged with their equipment. They were aged under a constant current, elevated temperature environment, with current of 150 mA and temperature of 100 °C. This temperature was chosen to avoid inducing material aging effects that have been observed at higher temperature aging (19). Quantum efficiency and threshold current were measured periodically during aging to monitor the evolution of the devices' performances.

3.6 Results

3.6.1 Spectral Results

Of the 11 devices studied, 10 had no changes in their spectra that could not be fitted to by adjusting gain and effective index parameters, and one device had a significant change that could not be fitted to by adjusting gain and effective index parameters.

The spectra of device 9 began changing after the laser subcarrier was bonded to the aging carrier, continued to change during burn-in, and stabilized before aging began. The change was observed as a shifting of FP modes with respect to the stopband position and a temporary increase in amplitude of the FP mode envelope.

3.6.1.1 Shifted FP Mode Positions

Front facet spectra from Laser 9, taken at different times of the study, are plotted in Fig. 3.2 with fits using the original facet parameter values determined in the original data set, showing the shifting FP mode position. Back facet spectra show similar trends. It is evident that the long wavelength FP modes are not aligned properly in three of the data sets when these fitting parameters are used.

This shifting of FP mode positions can be attributed to a change in the parameter δ from Eq. 2.2. The only variable in this parameter is the effective laser length, $L_{eff} = n_e \cdot L$. The effective laser length is a combination of five fitting parameters: $L_{eff} = n_e \cdot \Lambda \cdot ((\frac{\phi_{front}}{360} + \#\ grating\ periods) + \frac{\phi_{back}}{360})$, so a change in any of these parameters will shift the FP modes.

Isolating the changing parameter that caused the FP mode shift requires examination of the spectra around the stopband region in addition to the misaligned FP mode positions of the spectra. The spectra around the stopband region are very similar in all data sets, the only change in the spectra is the position of the FP modes with respect to the stopband position.

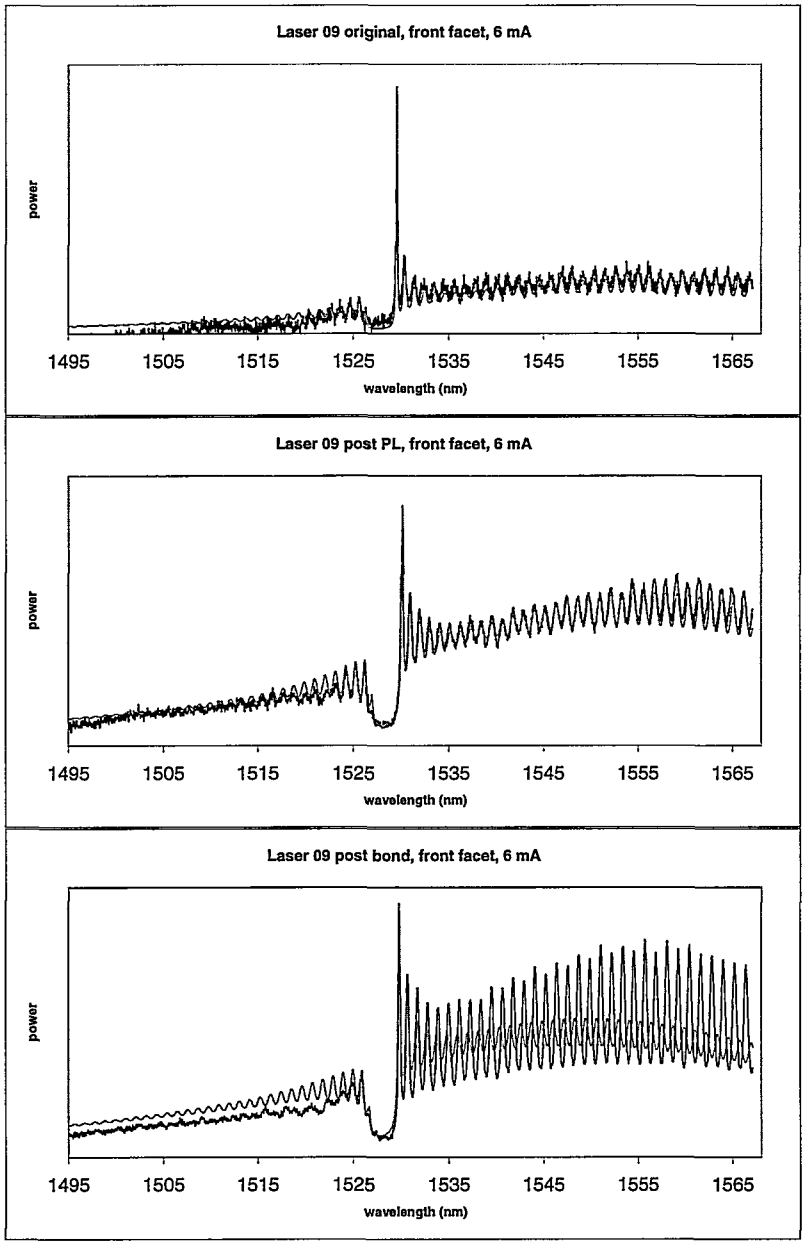

Figure 3.2: Laser 9 front facet spectra and fits with static facet parameters

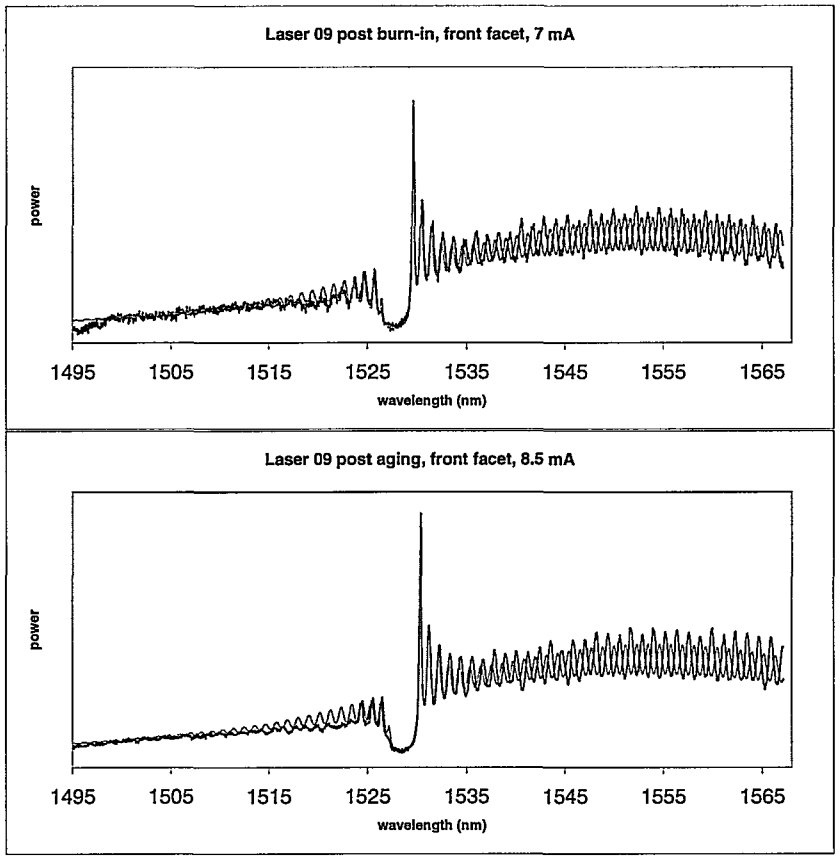

Figure 3.2: (continued) Laser 9 front facet spectra and fits with static facet parameters

This similarity shows that the effective index isn't the cause of the shift, as a uniform change of effective index along the laser cavity would shift the FP modes and the stopband position by an identical amount. Similar reasoning eliminates the possibility of a change in the grating period length (Λ) from causing the shift.

Changes in the number of grating periods of the laser can be eliminated as a cause

for the shifting FP positions since; for one, that change is physically impossible; and two, grating period numbers are integer values, each one equivalent to 360° of facet phase. As discussed in Section 3.5.1.2, a change of 360° of facet phase shifts the FP modes by one whole FSR, which does not account for the fractional FSR shift that is observed in the spectra.

Finally, the similarity of the data sets' spectra around the stopband region eliminates the possibility of ϕ_b changing, since changes in that facet are evident in the spectra close to the stopband region, as discussed in Section 3.5.1.1.

By the above reasoning, only ϕ_f remains as a possible parameter in this model that can account for the spectral changes that were observed.

3.6.1.2 Increased FP Envelope Amplitude

To account for the increase in the FP mode envelope amplitude in the post bond data set, $R_f \cdot R_f \cdot G$ has to be increased. As discussed in Section 3.5.1.2, an increase in gain would change the ratio of the intensities of the lasing peak to its sidemodes, which was not observed in the measured spectra. Also, as discussed in Section 3.5.1.1, the similarity of the data sets around the stopband region of the spectra makes it unlikely that the back facet reflectivity is changing. Therefore, it is probable that the observed increase in FP mode envelope amplitude is caused by a change in R_f.

3.6.1.3 Fits Using Modified Facet Parameters

To test this hypothesis, the fitting algorithm was executed while allowing the front facet phase and reflectivity to vary at each data set. The results of these fits are plotted below in Fig. 3.3. It is obvious that these variable facet parameters make a far better fit to the spectral data than the static parameters whose fits were plotted in Fig. 3.2.

These fitted facet parameters are tabled below in Table 3.1. These results show that the front facet changed during the bonding of the laser carrier to the aging carrier, and stabilized after the burn-in period was completed.

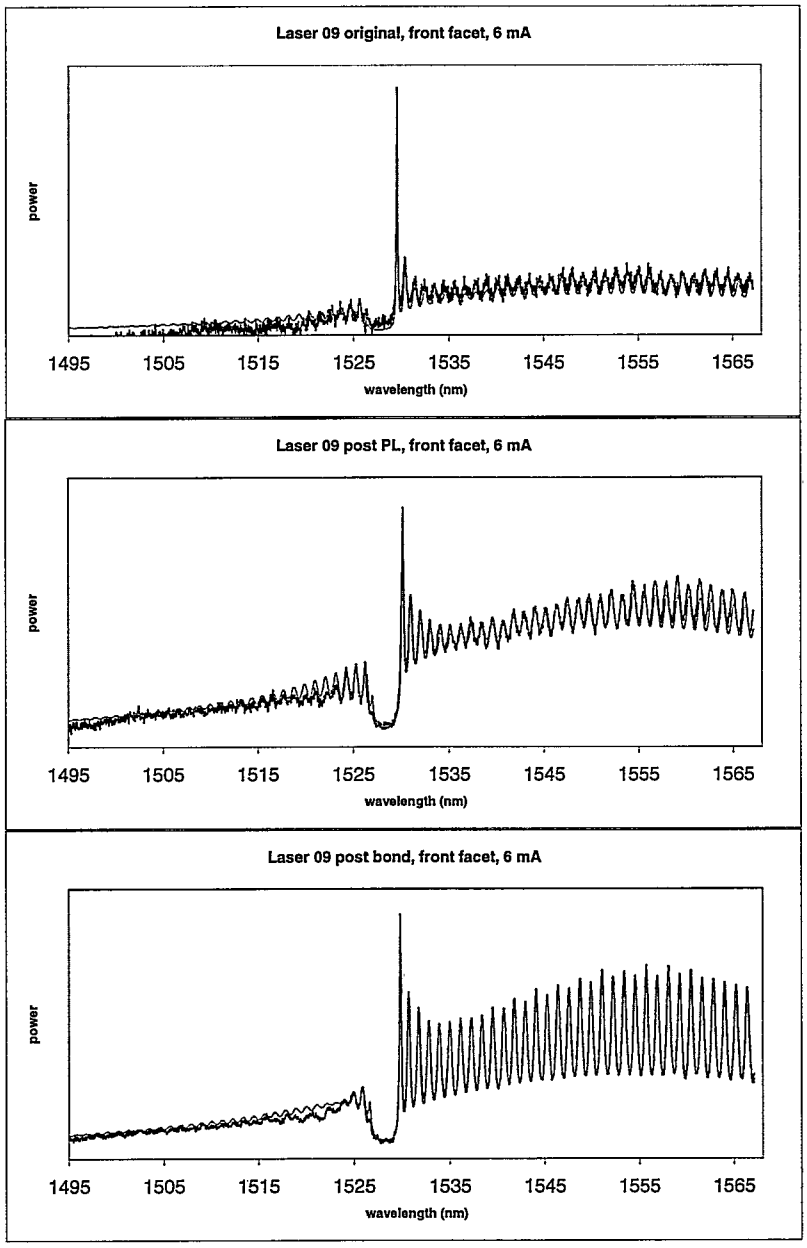

Figure 3.3: Laser 9 front facet spectra and fits with varying facet parameters

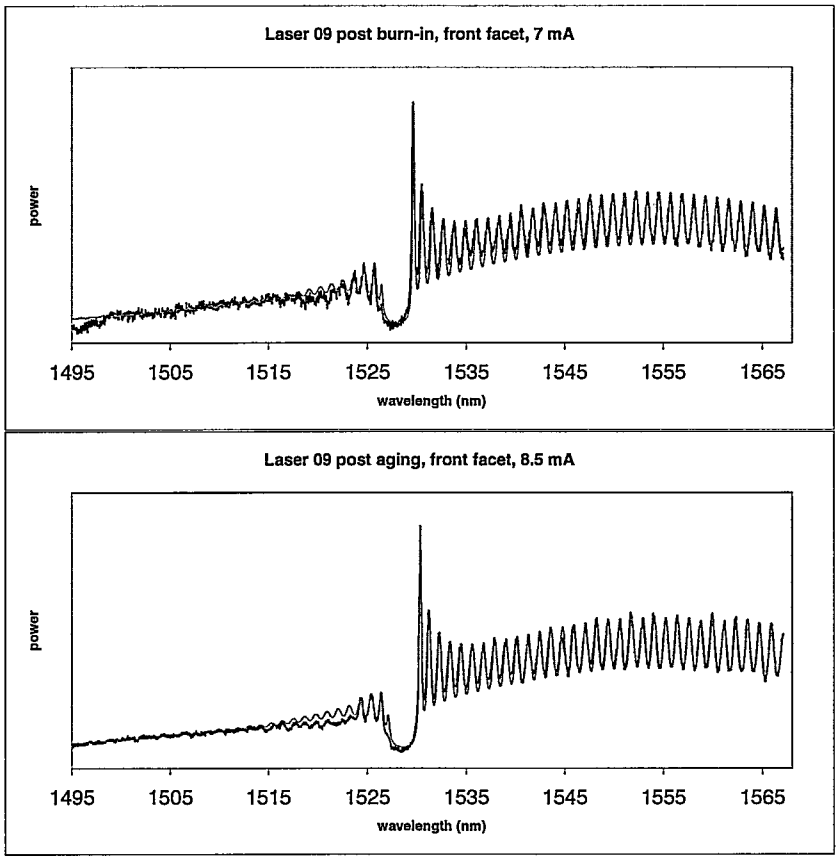

Figure 3.3: (continued) Laser 9 front facet spectra and fits with varying facet parameters

Laser 9	original	post PL	post bond	post burn-in	post aging
$\phi_f(^\circ)$	**20** $\pm$ 10	**20** $\pm$ 10	**176** $\pm$ 10	**234** $\pm$ 10	**234** $\pm$ 10
$\phi_b(^\circ)$	185 $\pm$ 5	185 $\pm$ 5	185 $\pm$ 5	185 $\pm$ 5	185 $\pm$ 5
$R_f(\%)$	0.7 $\pm$ 0.1	0.7 $\pm$ 0.1	**2.2** $\pm$ 0.1	0.7 $\pm$ 0.1	0.7 $\pm$ 0.1
$R_b(\%)$	91 $\pm$ 5	91 $\pm$ 5	91 $\pm$ 5	91 $\pm$ 5	91 $\pm$ 5

Table 3.1: Fitted facet parameters for laser 9

3.6.2 PL Measurement Results

All 11 devices that were measured had similar aging effects observed. As expected, there was a reduction in the level of reverse burning, and evidence of some stress relaxation.

To determine if the facet phase change in laser 9 that was fitted to in the previous section is a physical change that can be observed with DOP measurements, comparison between DOP measurements of laser 9 and the other lasers was done. DOP maps of laser 9 are shown in Fig. 3.4. All DOP maps are plotted from data taken by Sam K.K. Lam.

DOP maps are shown from the initial scans that were done before bonding of the lasers to the aging carriers and from the final scans that were done after 900 hours of aging. Two maps are shown for each measurement period, a coarse resolution that covers most of the device's facet, and a finer resolution that zooms in towards the active region area. Comparison of these results with those of a device that did not have detectable spectral changes is presented using DOP maps of laser 8 in Fig. 3.5. These maps are a good representation of the results from the other nine devices as well.

A dip is apparent in the post-aging DOP map of laser 9 between the two peaks near the active region. This is not seen in the DOP maps of the other devices. A horizontal profile across that region, 5 μm from the top of the scan, is plotted in Fig.

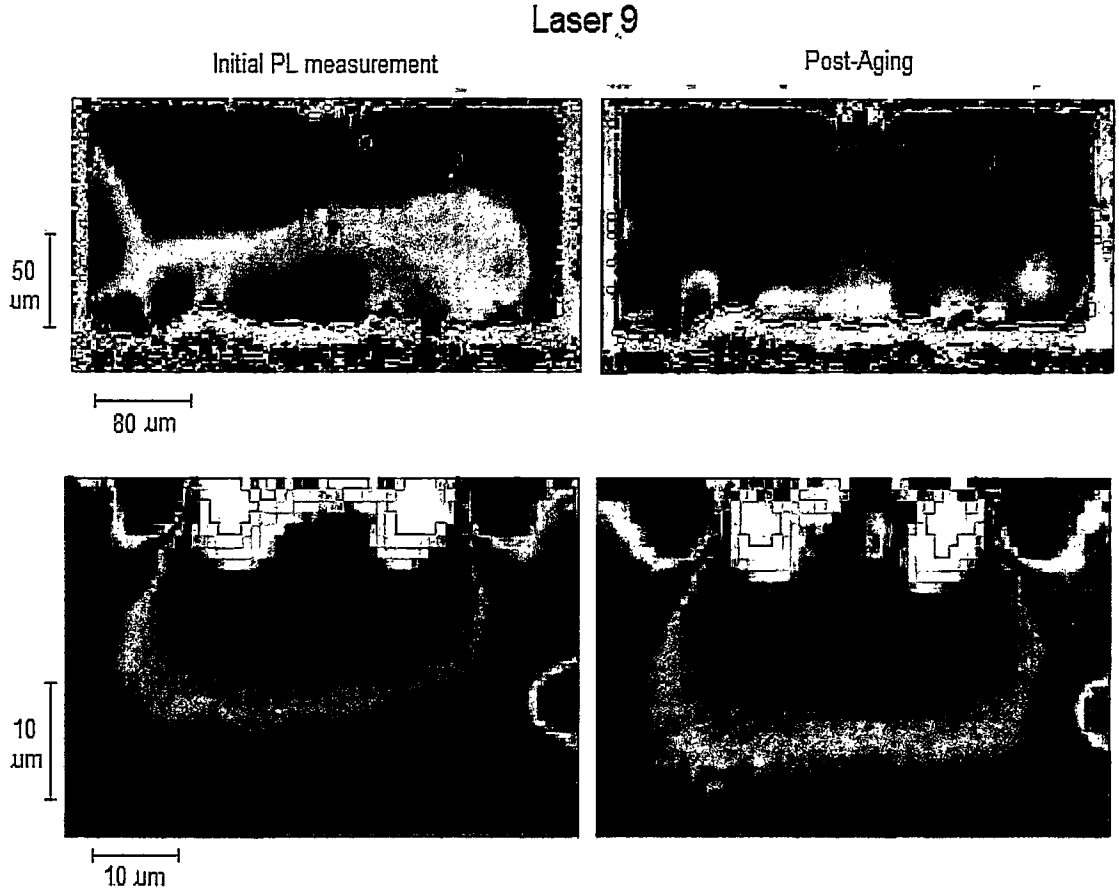

Figure 3.4: Laser 9 front facet DOP map, initial and post-aging measurements

3.6 for closer examination of the dip.

The PL scanning data had no observable differences between the devices.

3.6.3 Aging Data

Of the 11 lasers used in this study, 7 passed the aging process and 4 failed. A failed device is one whose operating characteristics fall outside of the set range of tolerances.

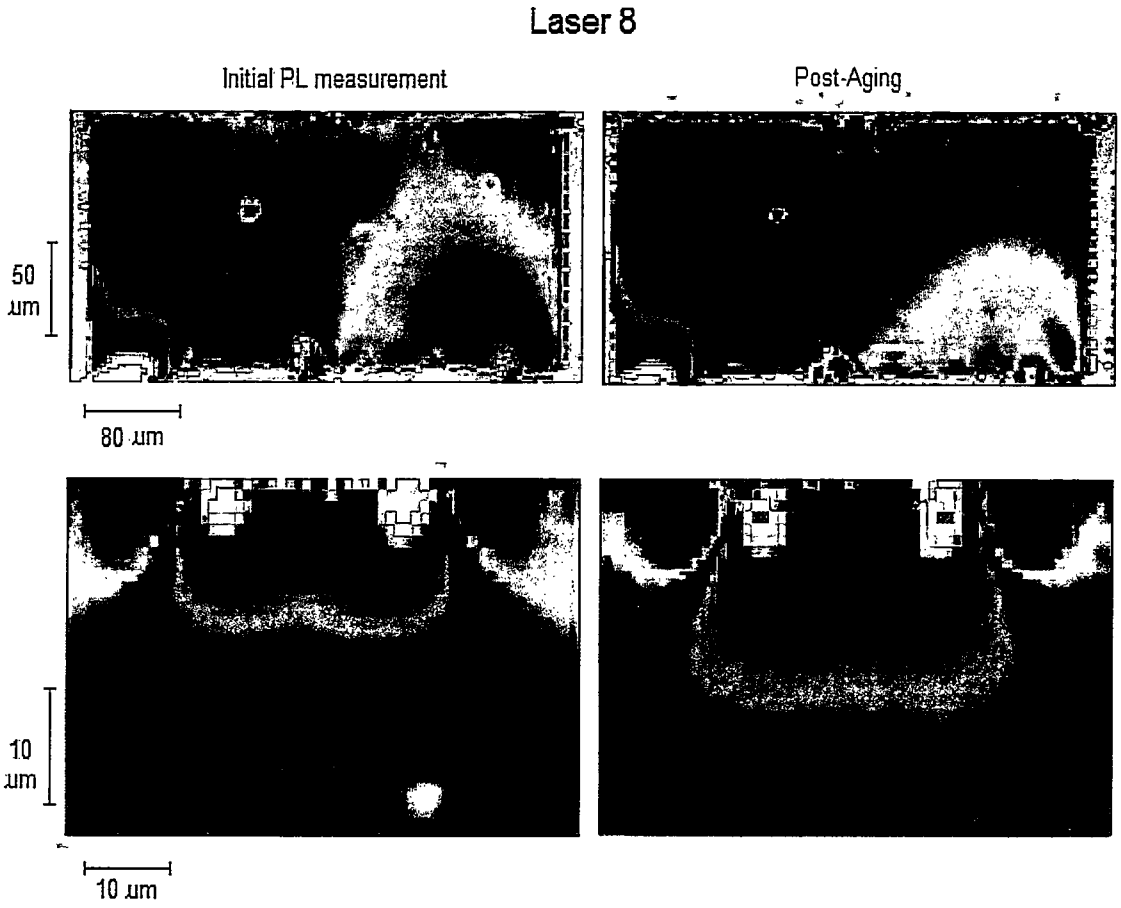

Figure 3.5: Laser 8 front facet DOP map, initial and post-aging measurements

In the case of these devices, this telerance level is where the threshold of the devices rises above 1.5× their initial values.

The evolution of threshold current with aging time is shown below in Fig. 3.7, and the evolution of quantum efficiency with aging time is shown below in Fig. 3.8.

These data sets begin after the 24 hour burn-in period was completed, and do

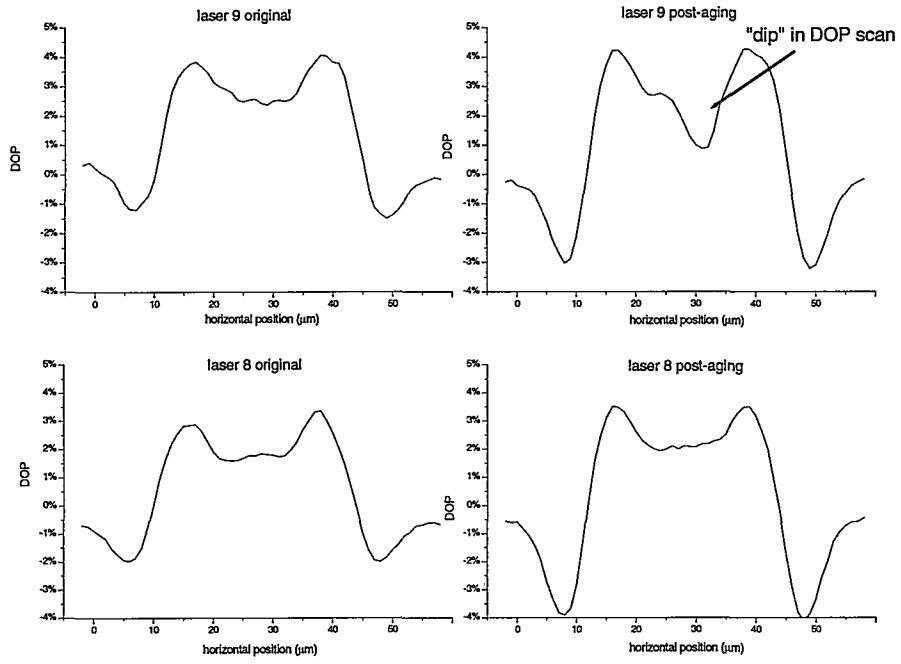

Figure 3.6: 2-D DOP profiles of laser 8 and 9 from high resolution maps, initial and post-aging measurements

not show the evolution during burn-in. When the burn-in period began, all devices had threshold currents of roughly the same value ($\sim$ 10 mA). It is seen in Fig. 3.7 that four devices had their threshold currents exceed the limit of 1.5$\times$ their initial threshold during the burn-in period. These four failed devices were all of the same batch, indicating a problem during manufacturing of this batch of devices. Figure 3.8 shows a constant, gradual decrease in quantum efficiency for all the devices, and

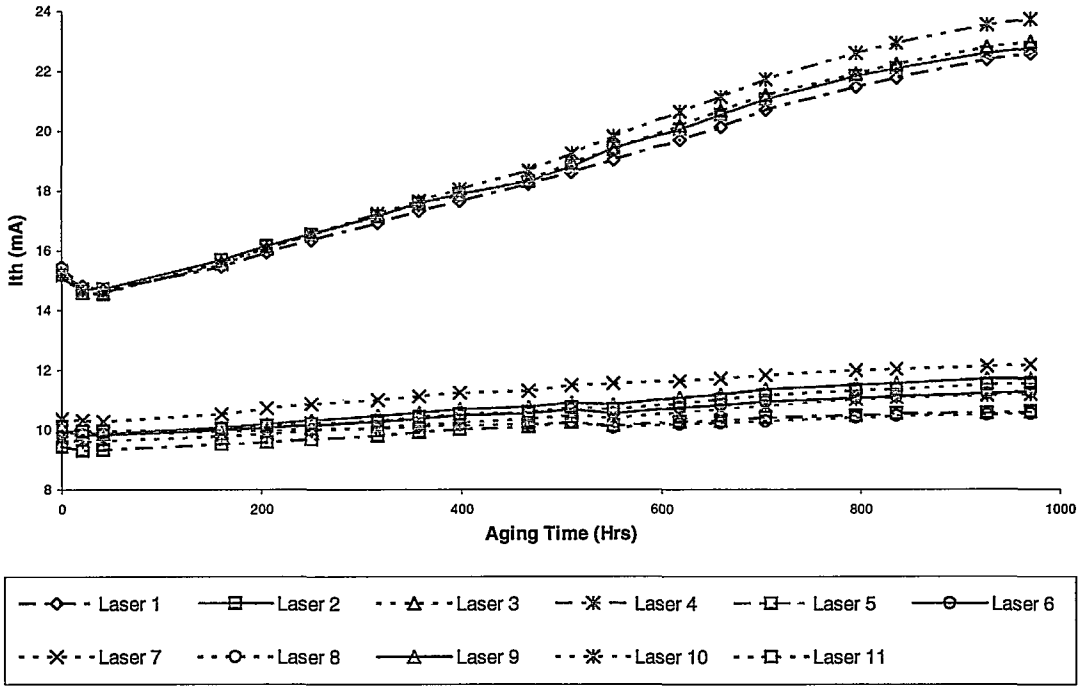

Figure 3.7: Evolution of threshold current with aging time

a small, abrupt increase at approximately 550 hours of aging. This one time change is assumed to be caused by a systematic effect during measurement that affected all devices simultaneously in a similar way.

All devices were kept in the study, regardless if they failed or passed the aging process. The failed devices remained able to operate and emit measurable spectra, but did so outside of their intended tolerances.

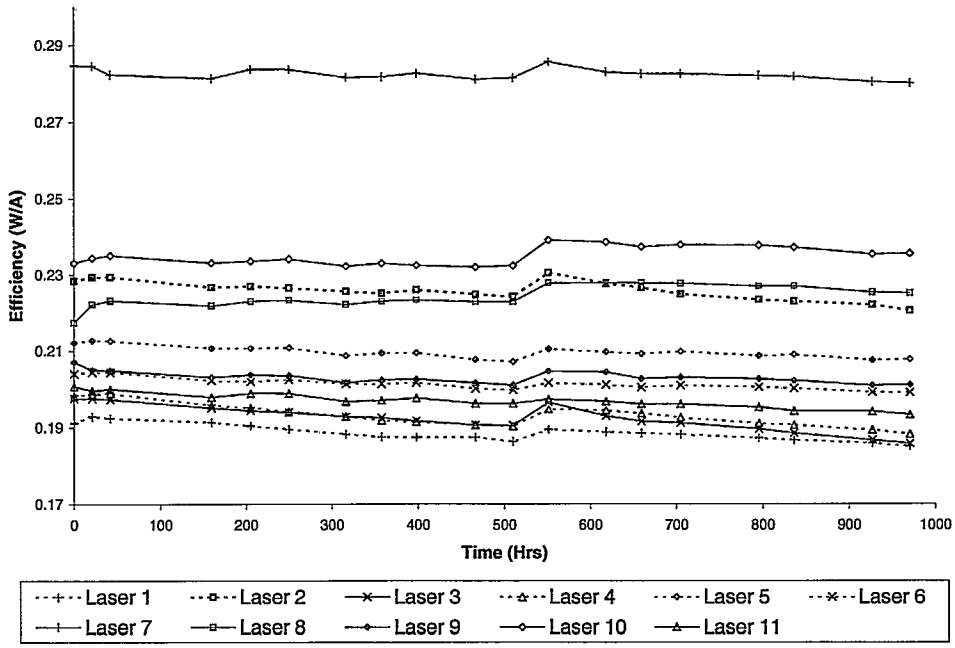

Figure 3.8: Evolution of efficiency with aging time

3.7 Discussion

Although the fits of laser 9's spectra using varying front facet parameters were good, it is unlikely that a laser facet phase would change by such a significant amount. A phase change of 215° is equivalent to an addition of 142 nm of material to the front facet. It is unlikely that a facet could add this much material without obvious changes being seen in the PL maps of the facet.

One possible alternate explanation of the spectral changes is through stress induced changes of index throughout the laser cavity (20). This idea is possibly supported by the DOP data that showed a slight difference in DOP of laser 9 to the rest of the devices. Such changes would create a non-uniform longitudinal index profile, and would affect the spectrum in unknown ways. This idea is presently being explored.

Chapter 4

Measuring Linewidth Enhancement Factor

4.1 The Linewidth Enhancement Factor

Distributed feedback (DFB) laser diodes are widely used for their single longitudinal mode operation, and narrow lasing linewidth. However, this narrow linewidth of continuous wave (CW) operated lasers is significantly broadened when the laser is current modulated, producing severe dispersion penalties when operated in WDM communication systems. This broadening of the time-averaged laser spectrum is known as frequency "chirp", and is caused by the variation of the laser's refractive index with modulated carrier density.

The linewidth enhancement factor α is an important parameter for characterizing the dynamic behaviour of semiconductor lasers. As defined by Henry (21), α is the ratio of the change of the real part of the refractive index caused by a change in carrier density to the change of the imaginary part of the refractive index to the same

change in carrier density:

$$\alpha = \frac{\Delta n'}{\Delta n''}. \tag{4.1}$$

This coupling between the carrier-induced variation of real and imaginary parts of the refractive index enhances the linewidth of semiconductor lasers from the value predicted from the phase fluctuation induced Schawlow-Townes linewidth (22) by a factor of $(1+\alpha^2)$ (21).

The LEF describes the amount of frequency chirp induced in a directly modulated laser diode, as it indicates that the carrier induced change in the imaginary part of the refractive index ,$\Delta n''$, also alters the real part of the refractive index by $\Delta n'$. $\Delta n'$ modifies the round trip cavity condition of the laser, thus shifting the lasing frequency from its steady state value. This frequency shift is called frequency chirp.

Analysis of Fabry-Perot laser diode (FPLD) dynamic behaviour using rate equations and small signal approximations leads to a simple expression relating α to the frequency and intensity modulation indices $\beta = d\nu/\nu_m$ and $m = dI/I$, respectively:

$$\frac{\beta}{m} = \frac{\alpha}{2}\sqrt{1+\left(\frac{\Gamma_g}{\omega_m}\right)^2}, \tag{4.2}$$

with $\Gamma_g = R_{sp}/S + \kappa_s S/\tau$ the damping rate of the laser, and ω_m the angular modulation frequency(23)(24). R_{sp} is the spontaneous emission rate, S is the photon density, κ_s is the gain compression coefficient and τ is the photon lifetime.

The derivation of this expression requires that the optical guiding layer of the

laser has a linear, spatially uniform susceptibility. If $\omega_m >> \Gamma_g$, then the expression simplifies to the widely used equation $|\alpha| = \frac{2\beta}{m}$.

These modulation indices can be measured experimentally (25)(26), and α can be determined by fitting the experimental results to the above expression.

Henning and Collins reported an alternate method of determining α, whereby α is calculated from measurements of the wavelength shift and modal gain of a FPLD at different injection currents to obtain $\Delta n'$ and $\Delta n''$ (27). This method is based upon finding the modal gain of the FPLD using the Hakki-Paoli expression: $G = 1/L \cdot ln\left([\sqrt{(}r_i) - 1]/[\sqrt{(}r_i) + 1]\right)$ (28), where r_i is the ratio of peaks to valleys of a FPLD spectrum.

These two approaches for determining alpha have been used widely since their discoveries, and other measurement methods have been created based upon the initial findings of Harder, Valhala and Yariv and of Henning and Collins (23)(29).

4.1.1 Linewidth Enhancement Factor in DFB Lasers

When examining the LEF of DFB lasers, the analysis isn't as straightforward as for FPLDs. In FPLDs the round trip phase change induced by carrier density changes is solely due to the change of effective device length through the material properties, while in DFB lasers the round trip phase change is also affected by changes in structural parameters such as the frequency dependant distributed Bragg reflector (30), and the interaction of the laser facets with the Bragg reflector (8)(31). By adjusting

the properties of the Bragg reflector, the carrier induced round trip phase change can be modified, leading to low chirp and spectral linewidth performances of DFB devices. For this reason, the usual α parameter used for characterizing FPLDs is replaced by an effective linewidth enhancement factor, α_e, for characterizing DFB lasers (32). This effective LEF generally accounts for influences such as complex coupling in the grating (30)(33) and wavelength detuning (32)(34)(35)(36)(37), each of which act to change the measured linewidth of the device from that calculated using the unmodified material α.

The nature of the distributed feedback mechanism of the laser, which is a longitudinally varying susceptibility, is sensitive to spatial holeburning (SHB) effects. This sensitivity necessitates a further adjustment factor to α_e. Spatial holeburning has the effect of inducing local variations of the Bragg wavelength along the laser cavity, and since the distributed feedback (and the resulting spectrum of the laser) depends on this Bragg wavelength, any dynamic SHB effects must be included in a rigorous dynamic analysis of the laser.

Phenomenologically, an additional factor (α_{SHB}) is introduced in the dynamic analysis that accounts for the effect that the SHB in the laser has on the feedback loss, and the lasing peak position, in the laser cavity. The dynamic effect that α_{SHB} has on the FM response spectrum can be determined through a similar analysis as was done for FPLDs by combining the effect of both α_e and α_{SHB} together to obtain

a modified effective linewidth enhancement factor α_{em} that is device dependant. This modified effective linewidth enhancement factor is the term that is of relevance to designers wanting to know the level of frequency chirp that a particular DFB device will have.

The parameter α_{SHB} is related to the level of SHB in the laser and so its effect on the lasing frequency, $\Delta\nu_{SHB}$, will work in phase with the current modulation in the laser. Its amplitude is device dependent, depending on how the laser's SHB profile affects the feedback of that particular laser, and is frequency dependant, rolling off at high frequencies due to finite carrier lifetimes.

The phase relationship between field intensity, carrier density, real refractive index, imaginary refractive index, $\Delta\nu_\alpha$ and $\Delta\nu_{SHB}$ are tabulated below in Table 4.1 for a laser modulated above steady state frequencies. The value of $\Delta\nu_{SHB}$ (amplitude and sign) will depend on how the SHB profile in a particular device's cavity affects its lasing frequency. For example, if a device's SHB profile acts to shift the lasing mode to lower frequencies, then $\Delta\nu_{SHB}$ acts 180° to $\Delta\nu_\alpha$. The total frequency chirp (due to α_{em}) is the sum of both $\Delta\nu_{SHB}$ and $\Delta\nu_\alpha$, and for a laser of this type, it would be lower than expected from considering α_e only.

	$\lvert E\rvert^2$	N	n_R	n_i	$\Delta\nu_\alpha$	$\Delta\nu_{SHB}$
phase relative to $\lvert E\rvert^2$ (rad)	0	$\pi/2$	$-\pi/2$	$\pi/2$	$\pi/2$	$\pm\pi/2$

Table 4.1: Phase relation of dynamic laser parameters with respect to photon intensity

This rigorous treatment of the dynamics of DFB lasers that includes SHB effects on the FM response, has been tackled recently with the use of sophisticated computer simulations (38)(39)(40), and it has been found that spatial holeburning can affect the feedback enough to cause observable differences between the FM response of similarly manufactured DFB lasers.

The level of influence that α_{SHB} will have for a particular device is not easily computed, since its value depends on the SHB profile within the laser, which depends on the random facet phases/reflectivities of the DFB laser (5). Therefore, without knowledge of laser the facet properties, it is impossible to calculate the effect of α_{SHB}. Due to this problem, it is often difficult to predict accurately the FM characteristics of individual DFB laser diodes (38).

With the recent advent of computer programs that can fit below threshold laser spectra to mathematical models of the laser (2), thereby extracting a laser's physical parameters from its measured spectrum, a laser's facet properties can be determined non-destructively. Using these parameters, the above threshold carrier distribution can be calculated, and the effect that this SHB has on the feedback loss of the laser cavity (α_{SHB}) can then be determined.

4.2 Experimental Details

We designed an experiment to measure the combined effect of α_e and α_{SHB} on the FM characteristics of 4 DFB laser diodes, hoping to determine the effect of α_{SHB} by comparing the FM responses of the lasers. Differences in α_{SHB} between the four lasers will be manifested as differences in the FM response curves of the lasers (38).

These lasers were chosen from the same batch to minimize the variation between them to facet phase and reflectivity. The lasers were HR (R = 70-80%) coated on one facet, AR (5-15%) coated on the other, mounted p-side up and wire bonded to an aluminum nitride carrier.

4.2.1 Determination of Modulation Indices

An intensity and frequency modulated optical wave can be written in its complex representation:

$$E(t) = E_o(1 + M\cos(\omega_m t))e^{[i(\omega_o)t+\beta\cos(\omega_m t+\theta)]},$$

with E_o the continuous wave field intensity, ω_m the modulation frequency, $M = \Delta I/I$ the amplitude modulation index, $\beta = \Delta\omega/\omega_m$ the frequency modulation index, and θ the phase between the amplitude and frequency modulation.

This expression can be expanded into its frequency components using the Jacobi-Anger expansion (41). Expanding to third order in J, a general expression for E/E_o is found to be:

centre frequency: $\sqrt{A^2 + (MB)^2} \cdot \cos(\omega_m t)$

1st upper/lower sidebands: $\sqrt{(\mp B \pm \frac{M}{2} D)^2 + (\pm C + \frac{M}{2}(E + A))^2} \cdot \cos(\omega_o t \pm \omega_m t)$

2nd upper/lower sidebands: $\sqrt{(E \pm \frac{M}{2} C)^2 + (D \pm \frac{M}{2} B)^2} \cdot \cos(\omega_o t \pm 2\omega_m t)$

with

$A = J_0(x)J_0(y) - 2J_2(x)J_2(y)$

$B = J_1(x)J_2(y) - J_1(x)J_0(y) - J_3(x)J_2(y)$

$C = J_0(x)J_1(y) - J_2(x)J_1(y) + J_2(x)J_3(y)$

$D = J_3(x)J_1(y) - J_1(x)J_1(y) - J_1(x)J_3(y)$

$E = J_0(x)J_2(y) - J_2(x)J_0(y)$

and

$x = \beta\cos(\theta), y = \beta\sin(\theta)$

These expressions can be simplified if the modulation index is small enough for small signal approximations to be valid so that $\beta < 1$, and if we consider frequencies where the phase between the carriers and photons is $\theta = \pi/2$. Under these conditions, the expressions for E/E_o are simplified to the following:

centre frequency: $J_0(\beta) \cdot \cos(\omega_m t)$

1st upper/lower sidebands: $\pm[J_1(\beta) + \frac{M}{2}(J_0(\beta) + J_2(\beta)] \cdot \cos(\omega_o t \pm \omega_m t)$

2nd upper/lower sidebands: $[J_2(\beta) \pm \frac{M}{2}(J_1(\beta) + J_3(\beta))] \cdot \cos(\omega_o t \pm 2\omega_m t)$

It can be seen that if a modulated laser's spectrum is measured, the AM and FM indices can be determined by fitting the spectra to these expressions.

4.2.2 Experimental Setup

The lasers in our study were current driven on a copper block, temperature controlled to 0.1 °C using a McMaster analogue PID feedback controller, and modulated using a HP network analyzer 8719C (0.05-13 GHz). The electrical signal was coupled into the laser diode by terminating the coaxial transmission line from the network analyzer with a Sub-Miniature A (SMA) microwave connector that was brought in contact with a 50 Ω resistor soldered to a copper block that the laser and submount were supported on. The tongue contacted the p-side contact of the submount, while the copper block contacted the n-side contact of the submount. This setup allowed adequate modulation power to be transmitted over the entire frequency range of the network analyzer. A diagram of this signal coupling is shown below in Fig. 4.1

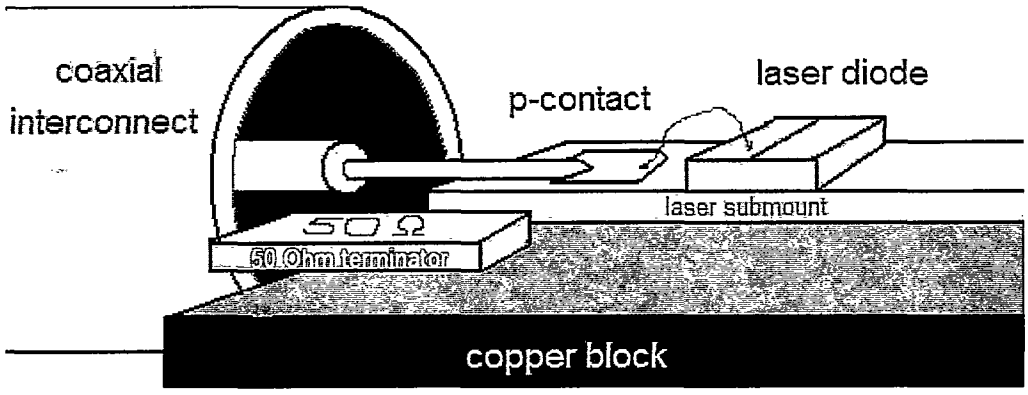

Figure 4.1: Setup for electrical coupling of network analyzer to laser diode

The modulated laser output was collected with a 1" F1 plano-convex lens, sent

through a Faraday optical isolator (Optics for Research) to minimize back reflections, collimated with a second 1" F1 plano-convex lens, and filtered using a Fabry-Perot scanning interferometer (Burleigh RC-110, finesse >40, free spectral range 500 MHz - 30 GHz). The transmitted light from the interferometer was focused with a third 1" F1 plano-convex lens through a 150 μm pinhole, to maximize the finesse of the fringes, that was mounted on an InGaAs detector. A diagram of this setup is shown in Fig. 4.2

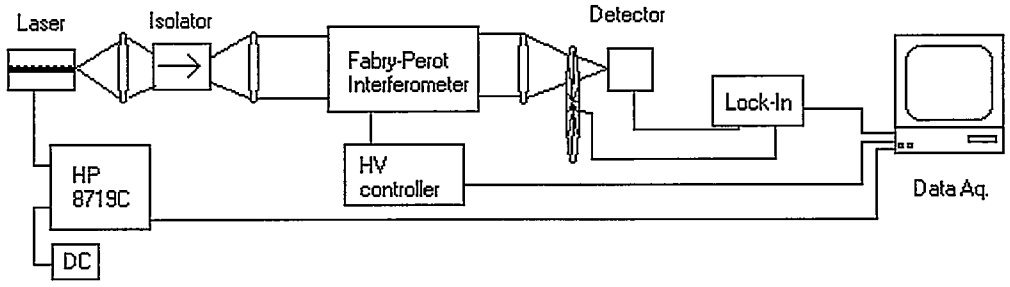

Figure 4.2: Experimental setup to measure modulated laser chirp

By scanning the interferometer's mirror spacing through a few free spectral ranges and using a lock-in amplifier to record the detector signal, we were able to resolve the spectra's sidebands and record the modulated spectra for analysis.

The modulation power was adjusted at each bias and frequency so that $0.1 < M <$

0.2 to ensure that sidebands were observable while keeping the modulation in the small signal regime and avoiding clipping of the laser below threshold. By adjusting the modulation power for each laser at each bias to obtain a desired interferometer output, calibration of the system's power transmission was unnecessary. Calibration is required if one obtains readings from the network analyzer directly, but in our case values of the transmitted modulation power can be determined by extracting the AM index from the interferometer output. This approach greatly simplified the data acquisition process from one that requires transmission line calibration. If such a calibration procedure were required, it would have to be performed each time a laser was connected to the system, and would introduce much experimental uncertainty to the measurements.

4.2.3 Data Analysis

The spectra were recorded using a McMaster lock-in amplifier automated using LabView software. Each data set contained a continuous wave spectra of the laser, taken to represent the FP interferometer transmission function. The modulated spectra were then deconvolved with this transmission function to obtain sideband and carrier intensities. Deconvolution is required to remove the contribution of a peak's tails from the amplitude of neighboring peaks. The process was performed using knowledge from the Bessel function expansion from Section 4.2.1 that the laser spectra

consists of very narrow linewidth peaks with constant wavelength spacing separating them. The transmission function of the interferometer was scaled approximately to each peak's intensity and wavelengths were aligned appropriately. These scaled transmission functions were then added together to form the fitted FP output. By iteratively adjusting the fitted intensities of the peaks according to the results from the previous fitted FP output, accurate values for the sideband and carrier intensities were obtained.

This method of deconvolution minimizes the effects of non-ideal optical alignment, since any deviation of the transmission function from its theoretical ideal shape is included in the CW spectra and accounted for in the deconvolution.

A demonstration of this deconvolution process is shown in Fig 4.3. The bottom plot shows the fitted delta function sideband intensities spaced at integer multiples of the modulation frequency, the middle plot shows the convolution of these sidebands with the FP transmission spectrum and the top plot shows the resulting summation of all sideband contributions, plotted with the original experimental FP spectral data. It is difficult to distinguish the two data sets in the top plot, and this demonstrates the accuracy of the deconvolution procedure. The mean deviation of the fitted and experimental data is $0.07\% \pm 0.90\%$.

Once these deconvolved sideband intensities were found, they were fitted to the

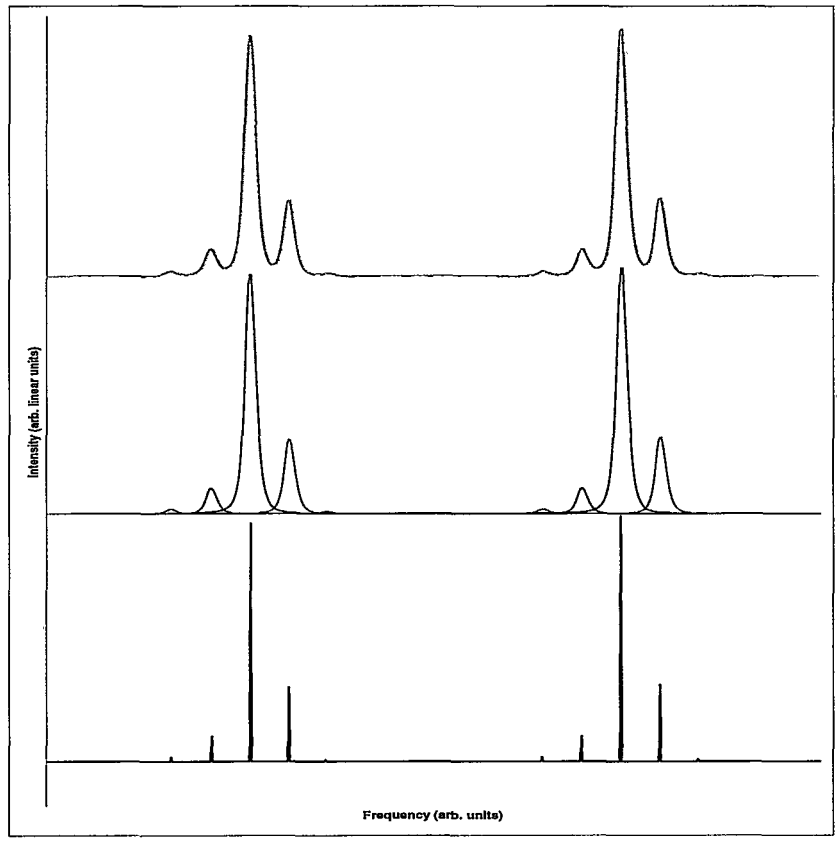

Figure 4.3: Deconvolution of spectrum by summation of FP transmission function.

simplified Bessel function expansion from Section 4.2.1 using a Marquardt least-squares fitting algorithm to determine values of M and β for the given data set. In order to avoid degenerate solutions of the fitted equations, $\theta = \pi/2$ is assumed for the fits, which justifies the use of the simplified Bessel function expansion. This assumption is expected to be valid from consideration of small signal analysis of rate equations that show that $\theta \simeq \pi/2$ for ω large enough that carriers aren't in phase with

current (42)(43). A number of samples were taken at each bias level and modulation frequency to provide statistics for experimental uncertainty, and using these samples, a mean and error value was calculated for each β/M data point.

4.3 Experimental Results

4.3.1 Fitted Laser Parameters

The four lasers had below threshold spectra taken as described in Section 3.5.1, and the data was fitted to as described in Section 3.5.1.2. The following laser facet parameter values were extracted, listed in Table 4.2. The definitions of all variables are the same as defined in Section 2.2.

	R_f (%)	R_b (%)	ϕ_f	ϕ_b
Laser 5	$13.3\% \pm 0.6\%$	$73\% \pm 4\%$	$141° \pm 10°$	$252° \pm 5°$
Laser 6	$5.7\% \pm 0.4\%$	$93\% \pm 5\%$	$203° \pm 10°$	$170° \pm 5°$
Laser 7	$7.6\% \pm 0.4\%$	$79\% \pm 4\%$	$-6° \pm 10°$	$245° \pm 5°$
Laser 8	$11.8\% \pm 0.6\%$	$74\% \pm 4\%$	$78° \pm 10°$	$286° \pm 5°$

Table 4.2: Fitted facet parameters from below threshold spectral data.

The differences between these four lasers' facets result in different longitudinal intensity distributions in each of the lasers' cavities. These distributions are shown below in Fig. 4.4, calculated using the transfer matrix model (5). In order to isolate the effect of facet parameters on intensity distribution, these distributions were calculated using the same parameter set while only adjusting the facet parameters $(R_f, R_b, \phi_f, \phi_b)$ for each laser.

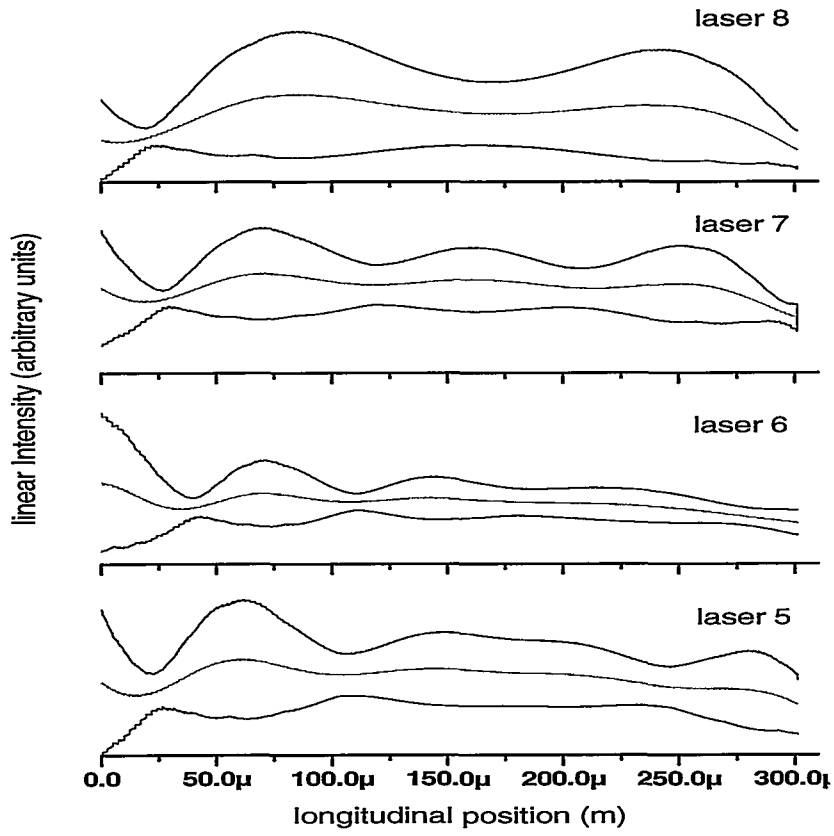

Figure 4.4: Calculated longitudinal intensity distributions for the four lasers studied. Envelope functions and average intensities of standing waves are plotted.

It can be seen in these plots that the longitudinal intensity distribution varies with facet parameters.

4.3.2 FM Response of the Lasers

FM response data was taken for the four lasers over a range of four bias currents. The results of these measurements were expected to show differences between the lasers (38) due to the different facet phases and reflectivites, and thus different α_{SHB} values

of the four lasers. These FM response spectra are plotted below in Fig. 4.5.

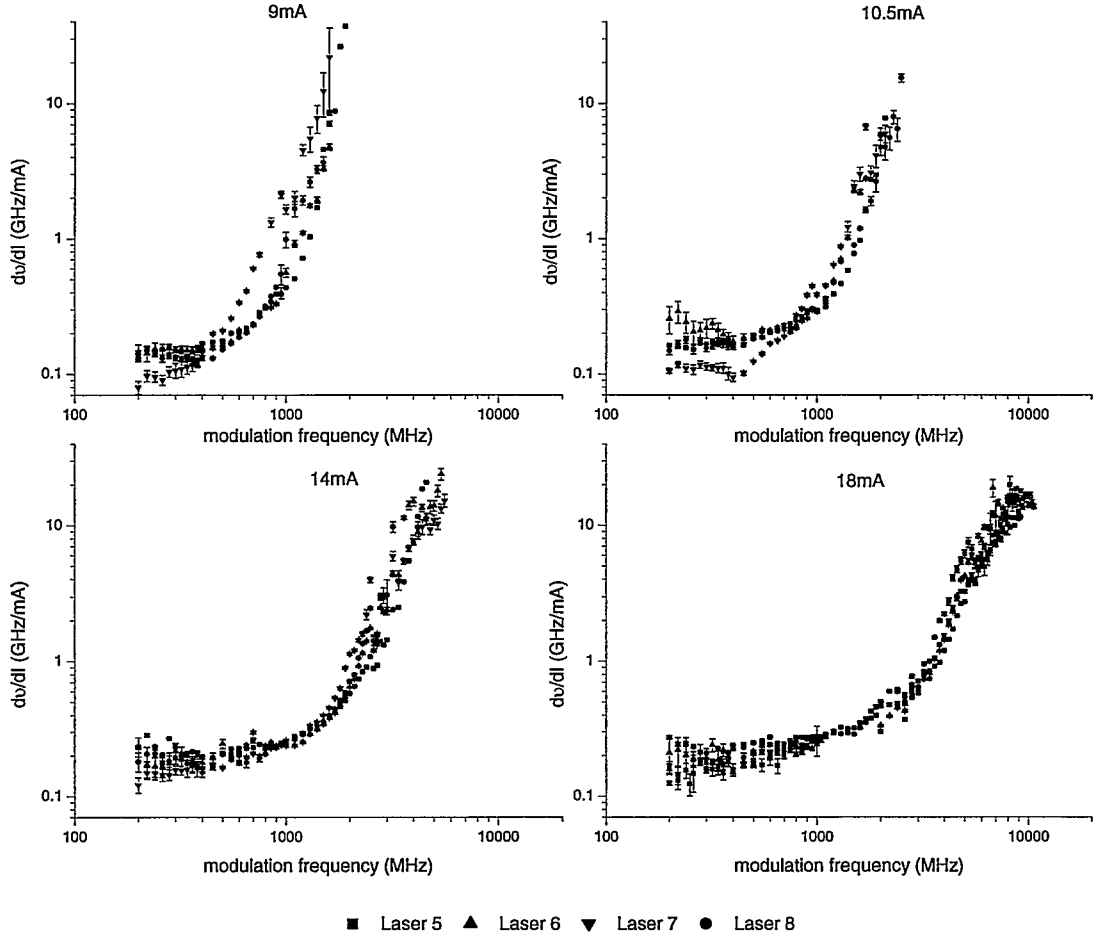

Figure 4.5: FM response spectra of four DFB lasers at four bias currents.

The responses of laser 7 are slightly different than those of the other three devices for bias levels of 9 mA and 10.5 mA. The difference at 9 mA bias is a uniform offset

of the curve towards lower frequencies that can be attributed to a higher threshold current lowering the amount of above threshold current that the device is pumped with. The difference at 10.5 mA bias is a section where the curve is not smooth, with a "kink" being seen at around 400 MHz. Other than these two features, it was found that the results were very similar between the four devices and within experimental uncertainty for most points, and so the effect of α_{SHB} on the FM response spectrum was determined to be unobservable for these lasers by the technique used.

These very similar FM responses can be attributed to two possible factors. Firstly, the α_e factors of the lasers could be too low to cause significant SHB effects on the feedback of the laser. If α_e is too small, then the SHB effect will also be small since the SHB induced feedback changes are dependant on the amount that α_e changed the refractive index. Secondly, the SHB profiles of the four lasers could be too similar to one another to cause significant differences in the lasers' α_{SHB} values. Although the envelope functions of the intensity distributions in Fig. 4.4 are different, the averaged intensities are fairly similar.

A low α_e is a reasonable hypothesis as can be deduced by observing the below threshold spectra of the lasers. The spectra of one of the four lasers is plotted below in Fig. 4.6. In this spectra, it is observed that the lasing peak will be on the short wavelength side of the gain peak (the stopband is located at $\sim$ 1530 nm while the gain peak is at $\sim$ 1550 nm). It is known that α decreases as one moves to smaller

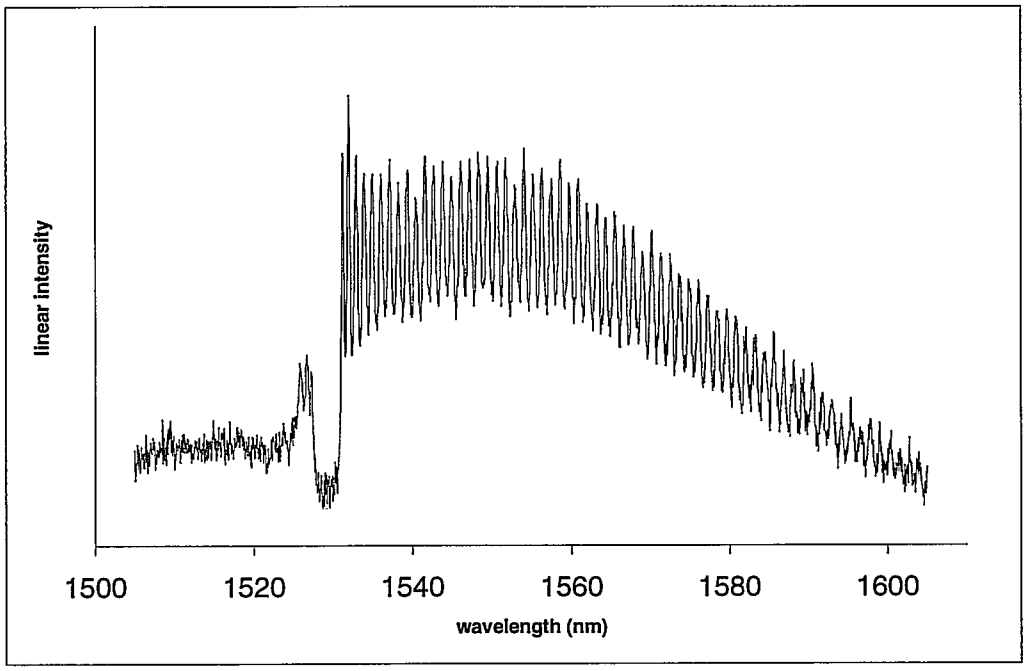

Figure 4.6: Below threshold wide-band spectrum of one of the lasers used in the study.

wavelengths from the gain peak wavelength (the wavelength detuning phenomenon) (32)(34)(35)(36)(37).

This phenomenon can be explained qualitatively by examining the shapes of differential gain and index curves. A differential gain curve is roughly symmetric, while a differential index curve has highest values on the short wavelength side of the gain peak, decreasing as wavelengths increase (44)(45). From Eq. 4.1 and using the relation of material gain to imaginary index, $gain = -4\pi/\lambda n''$, it can be seen that $\alpha = -\frac{4\pi}{\lambda}\frac{dn'/dN}{d(gain)/dN} \propto \frac{diff.index}{diff.gain}$. Qualitative plots of differential index, differential gain

and their ratio are displayed in Fig. 4.7.

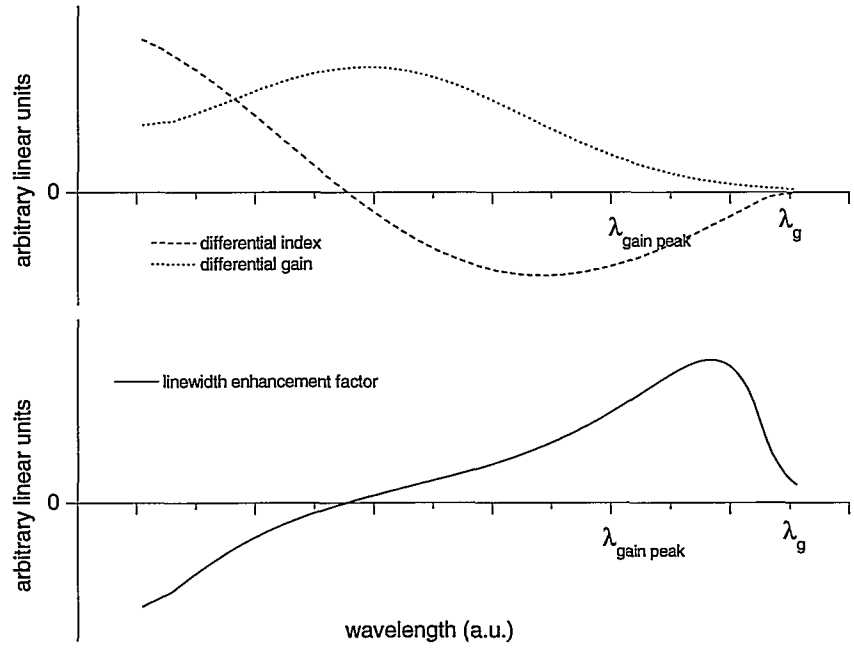

Figure 4.7: Qualitative curves of differential gain, differential index and resulting linewidth enhancement factor plotted against wavelength.

These plots show that in the wavelength region of the gain peak of the spectrum, α decreases for shorter lasing wavelengths. From this basic argument, it can be seen why the wavelength detuning phenomenon occurs.

4.3.3 Extraction of α Parameter

The α_{em} value of each laser was extracted from the modulation data by fitting the low frequency data to Eq. 4.2 using a Marquardt least squares algorithm. This expression is only valid for frequencies that are above dynamic thermal effects ($\sim$ 100MHz), and are below resonance frequency effects (dependant on device and bias level, ranges from $\sim$ 2 GHz to $\sim$ 10 GHz in our devices). Our data was taken at frequencies above dynamic thermal effects, and data taken at frequencies approaching the resonant frequency was excluded from the fitting.

The data was fitted to five unknowns: Rsp , κ/τ, Ith, α_{em} and $S_{multiplier}$, where $(I - Ith) \cdot S_{multiplier} = S$, assuming that photon density scales linearly with above threshold current. Units of Rsp, κ/τ and $S_{multiplier}$ were arbitrary since they divided each other out in the calculation. Each device's unknowns were fit simultaneously to data sets from four different bias levels. A sample plot of these fits is shown below in Fig. 4.8

The results of the four fits are tabulated below in Table 4.3.

	α_{em}	Rsp	κ/τ	Ith	$S_{multiplier}$	χ^2/dof
Laser 5	5.22 ± 0.08	3723 ± 2837	1.08 ± 0.02	5.86 ± 0.06	114 ± 2	1.29
Laser 6	5.15 ± 0.18	3125 ± 5708	1.07 ± 0.05	6.18 ± 0.14	113 ± 6	2.72
Laser 7	6.48 ± 1.32	0 ± 1925	0.92 ± 0.29	7.76 ± 0.27	101 ± 13	2.68
Laser 8	5.73 ± 0.11	0 ± 452	0.97 ± 0.03	6.55 ± 0.09	105 ± 4	3.22

Table 4.3: Fitted parameters of Eq. 4.2 from β/M data.

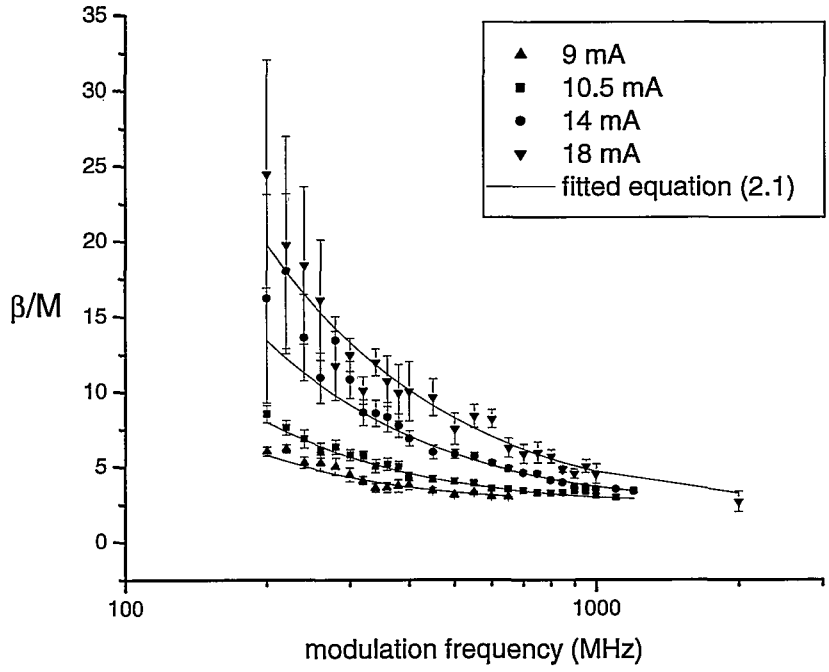

Figure 4.8: Sample plot of modulation data fitted to Eq. 4.2.

The variations in values for Rsp are reasonable since all values of Rsp/S are negligible compared to $\kappa S/\tau$ in Eq. 4.2 where $\Gamma_g = R_{sp}/S + \kappa_s S/\tau$.

4.4 Discussion

4.4.1 Discussion of FM Responses

The differences in laser 7's FM response spectra at 9 and 10.5 mA bias are the only obvious differences between responses of the four lasers. The difference at 9 mA bias

attributed to a higher threshold current in Section 4.3.2 was confirmed through fitting in Section 4.3.3. The difference at 10.5 mA, a "kink" in the curve at 400 MHz, could be the result of errors during spectral measurement, or could be caused by physical effects such as those caused by SHB. Further study is necessary to determine the significance of this kink.

4.4.2 Discussion of Extracted α Values

The four lasers show α_{em} values in the range of $5.0 < \alpha_{em} < 7.8$. Laser 7 had a far greater uncertainty in its α_{em} than the other three lasers, and is caused in part by the "kink" in its 10.5 mA curve that is not accounted for in the fitting equation.

The extracted values of α_{em} are not as small as would be expected in devices that are designed for low chirp (34). As described in section 4.1.1, since the measured LEF in a DFB laser is actually α_{em} and not α, it would be expected that α_{em} would be engineered to be lower than α that is usually in the range of $1 - 5$ (39).

The reason for such a high measurement of α_{em} may be attributed to a number of reasons.

Firstly, Eq. 4.2 used to extract the α parameter is highly simplified from what may be necessary for this particular application. One example of possible over-simplification is that Eq. 4.2 neglects carrier density effects that can be evident in quantum-well devices. The carrier density effect is caused by a current density

dependant α that increases with carrier concentration (39)(36). If this effect is significant in our devices, it would invalidate the fits which assume a constant α value with bias level.

Secondly, this analysis neglects the effect that the resonance peak in the FM spectrum has on the β/M spectrum. The resonance peak in the FM spectrum raises the asymptote floor that Eq. 4.2 shows β/M should approach at high frequencies. This has the effect of raising the fitted value of α from its actual value.

Thirdly, Eq. 4.2 assumes the phase between photon and carrier densities is constant at $\pi/2$. This assumption is valid from elementary dynamic analysis of carrier and photon rate equations (42); however, the approximations made in the rate equations may not be valid for a quantum well DFB laser with SHB. Dynamic SHB has been measured along the cavity of DFB lasers (46), and it was found that the phase between photon and carrier densities varies along the cavity between 0 and $\pi/2$, dependant on the SHB profile in the particular device. Such a deviation of the phase from $\pi/2$ affects the extracted β and M values, and would change the trend of β/M versus frequency that is used to fit α.

To demonstrate the effect of phase angle on the extracted β/M value, a modulated spectrum was fitted to the general Bessel function expansion over a range of phase angles. The results are plotted in Fig. 4.9 and show that as the phase changes from $\pi/2$, the extracted β/M value decreases from the value extracted assuming an angle

of $\pi/2$. Such a decrease in β/M over a range of higher frequency data points would result in a *lower* fitted α_{em} value than the true value.

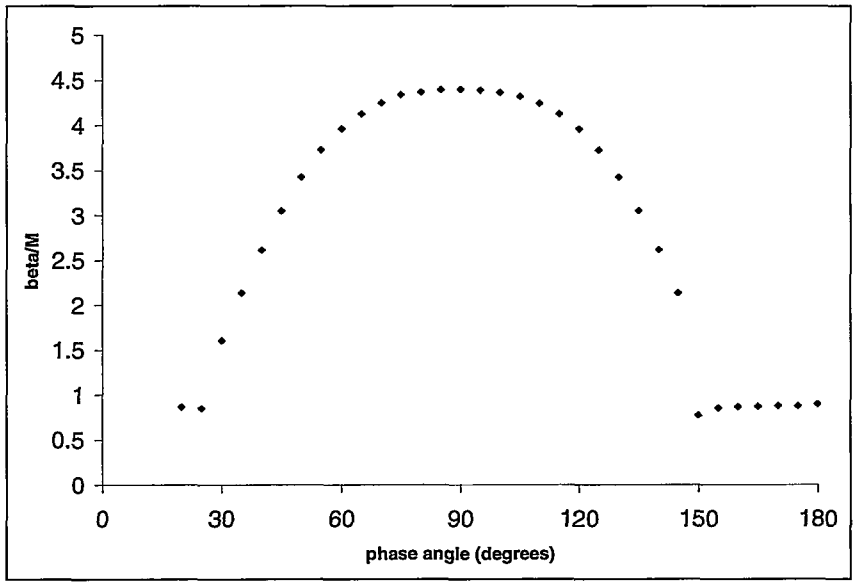

Figure 4.9: Variation of fitted β/M with changing phase angle between modulated carrier and photon densities.

It would be beneficial to compare a measurement of α using the method of Henning and Collins (27), perhaps using the Cassidy method (47) to determine the gain changes instead of the suggested Hakki-Paoli method (28). This method would only be valid at wavelength ranges far from the stopband, where the distributed feedback effects on the spectrum are minimal.

Chapter 5

Conclusions and Future Study Possibilities

5.1 Conclusions

This thesis examined DFB laser performance through two studies.

The transfer matrix method was fit to below threshold spectra during aging of devices to determine if facet aging effects could be observed. The devices' spectra were generally stable, with one exception. This device had a changing spectrum that was fitted to by varying the front facet parameters. Facet phase values changed from $20° \pm 10°$ to $234° \pm 10°$, and reflectivity temporarily changed from $0.7\% \pm 0.1\%$ to $2.2\% \pm 0.1\%$. Comparison to DOP measurements showed a unique stress pattern in the device's front facet that indicate changes in facet properties that may have caused the observed changes in the device's spectrum.

The FM response was measured from four devices to determine if facet variations between devices caused observable differences in the laser dynamics. Two differences

were noted, one being explained by differences in threshold current values, and one with unknown origin. The devices' modified effective linewidth enhancement factors were extracted from the FM responses. These values were higher then expected, and reasons for the high values were explored.

5.2 Opportunities for Future Study

This work has provided ample opportunity for further study.

It was shown that changes in below threshold spectra can be fitted to a simple physical model of the laser; however, the results do not seem physically possible. It would be useful to incorporate the effect of the observed stress on the longitudinal index profile of the laser cavity in the model. This possibly could provide a more physical explanation of the cause of the spectral changes that were observed.

It would be interesting to observe the facet changes using an additional technique; possibly a SEM measurement of laser 9's front facet could reveal the cause of the measurements that we observed.

Further aging of the devices, under more extreme conditions, could reveal material degradation effects that would be interesting to study through the below threshold spectral fitting procedure.

To obtain a better understanding of the physical conditions that are necessary to

reveal differences in α_{em} between devices, modifications of the existing above threshold model could be done. The model would have to solve the carrier and photon rate equations while calculating the spectra using the transfer matrix method to simulate the dynamic behaviour. A Runge-Kutta algorithm could be used to simulate a period of time that would reveal frequency chirp, although this could prove too time consuming for today's computers. An alternate method could be to simply model steady state spectra at high and low values of the current modulation, isolating the study to frequencies below where the effects of high frequency carrier rolloff occur.

Measuring α_{em} could be done using a different approach to determine if the results obtained in this study are valid. The Henning and Collins method (27) has been suggested, or fibre dispersion can be used to induce interferences between carrier and sideband frequencies that can be observed as resonance frequencies on a network analyzer (48).

Bibliography

[1] J. Kinoshita, "Modeling of high-speed DFB lasers considering the spatial hole-burning effect using three rate equations," *IEEE J. Quantum Electron.*, vol. 30, pp. 929–938, 1994.

[2] G.B. Morrison and D.T. Cassidy, "A probablility-amplitude transfer matrix model for distributed-feedback laser structures," *IEEE J. Quantum Electron.*, vol. 36, pp. 633–640, 2000.

[3] T. Erdogan, "Fiber grating spectra," *IEEE J. Lightwave Tech.*, vol. 15, pp. 1277–1294, 1997.

[4] G.B. Morrison and D.T. Cassidy, "A model for the above-threshold spectra of truncated-well distributed-feedback lasers," *IEEE J. Quantum Electron.*, vol. 39, pp. 279–288, 2003.

[5] G. B. Morrison and D.T. Cassidy, "A probability-amplitude transfer-matrix method for calculating the distribution of light in semiconductor lasers," *IEEE J. Quantum Electron.*, vol. 39, pp. 431–437, 2003.

[6] J.P. Weber and S. Wang, "A new method for the calculation of the emission spectrum of DFB and DBR lasers," *IEEE J. Quantum Electron.*, vol. 27, pp. 2256–2266, 1991.

[7] G.B. Morrison and D.T. Cassidy, "Improving the ability of a distributed feedback laser transfer-matrix model to fit to spectra from distributed-feedback lasers," *IEEE Photon. Technol. Lett.*, vol. 12, pp. 768–770, 2000.

[8] G.B. Morrison, D.T. Cassidy, and D.M. Bruce, "Facet phases and sub-threshold spectra of DFB lasers: Spectral extraction, features, explanations, and verification," *IEEE J. Quantum Electron.*, vol. 37, pp. 762–769, 2001.

[9] M.G. Boudreau, *Optical Coatings for Improved Semiconductor Diode Laser Performance*, Ph.D. thesis, McMaster University, 1997.

[10] G.H.B. Thompson, *Physics of Semiconductor Laser Devices*, John Wiley & Sons, 1980 p.197.

[11] M. Fukuda, *Reliability and Degradation of Semiconductor Lasers and LEDs*, Artech House, Inc, 1991.

[12] S.K.K. Lam, *To be submitted*, Ph.D. thesis, McMaster University, 2003.

[13] E.C. Freeman and W. Paul, "Optical constants of rf sputtered hydrogenated amophous si," *Phys. Rev. B*, vol. 20, pp. 716–728, 1979.

[14] H.A. Macleod, *Thin Film Optical Filters*, Adam Hilger Ltd, 1986.

[15] *Anritsu MS9710C Operation Manual*, Anritsu Corporation, 2001.

[16] P.D.Colbourne and D.T.Cassidy, "Bonding stress measurements from the degree of polarization of facet emission of AlGaAs superluminescent diodes," *IEEE J. Quantum Electron.*, vol. 27, pp. 914–920, 1991.

[17] Kenton White, "e-mail correspondance," 2002.

[18] P.D. Colbourne and D.T. Cassidy, "Imaging of stresses in GaAs diode lasers using polarization-resolved photoluminescence," *IEEE J. Quantum Electron.*, vol. 29, pp. 62–68, 1993.

[19] Greg Letal, "e-mail correspondance," 2003.

[20] M. Fritz, *To be submitted*, Ph.D. thesis, McMaster University, 2003.

[21] C.H. Henry, "Theory of the linewidth of semiconductor lasers," *IEEE J. Quantum Electron.*, vol. 18, pp. 259–264, 1982.

[22] A.L. Schawlow and C.H. Townes, "Infrared and optical masers," *Phys. Rev.*, vol. 112, pp. 1940–1949, 1958.

[23] K. Petermann, *Laser Diode Modulation and Noise*, vol. p.121, Kluwer Academic Publishers, Boston, MA, 1988.

[24] C. Harder, K. Vahala, and A. Yariv, "Measurement of the linewidth enhancement factor of semiconductor lasers," *Appl. Phys. Lett.*, vol. 42, pp. 328–330, 1983.

[25] S. Kobayashi, Y. Yamamoto, M. Ito, and T. Kimura, "Direct frequency modulation in AlGaAs semiconductor lasers," *IEEE J. Quantum Electron.*, vol. QE-18, pp. 582–595, 1982.

[26] O. Doyle, "Measuring modulus and phase of chirp/modulated power ratio," *Elec. Lett.*, vol. 23, pp. 133–134, 1987.

[27] D. Henning and J. Collins, "Measurements of the semiconductor laser linewidth broadening factor," *Elec. Lett.*, vol. 19, pp. 927–929, 1983.

[28] B. Hakki and T. Paoli, "Gain spectra in GaAs double heterostructure injection lasers," *J. Appl. Phys.*, vol. 46, pp. 1299–1306, 1975.

[29] R. Schimpe, J. Bowers, and T. Koch, "Characterisation of frequency response of 1.5 μm InGaAsP DFB laser diode and InGaAs pin photo diode by heterodyne technique," *Elec. Lett.*, vol. 22, pp. 453–454, 1986.

[30] K. Kudo, J.I.Shim, K. Komori, and S. Aria, "Reduction of effective linewidth enhancement factor of DFB lasers with complex coupling coefficients," *IEEE Photon. Technol. Lett.*, vol. 4, pp. 531–534, 1992.

[31] K. Kojima, K. Kyuma, and T. Nakayama, "Analysis of the spectral linewidth of distributed feedback laser diodes," *IEEE J. Lightwave Tech.*, vol. LT-3, pp. 1048–1055, 1985.

[32] G.Duan, P. Gallion, and G. Debarge, "Analysis of the phase-amplitude coupling

factor and spectral linewidth of distributed feedback and composite-cavity semiconductor lasers," *IEEE J. Quantum Electron.*, vol. 26, pp. 32–44, 1990.

[33] A.J. Lowery, "Large-signal effective alpha factor of complex-coupled DFB semiconductor lasers," *Elec. Lett.*, vol. 4, pp. 2295–2297, 1992.

[34] S. Ogita, M. Yano, H. Ishikawa, and H. Imai, "Linewidth reduction in DFB laser by detuning effect," *Elec. Lett.*, vol. 23, pp. 393–394, 1987.

[35] H.R. Choo, C.D. Park B. O, H.M. Kim, J.S. Kim, D.K. Oh, H.M. Kim, and K.E. Pyun, "Improvement of linewidth enhancement factor in 1.55 μm multiple-quantum-well laser diodes," *IEEE Photon. Technol. Lett.*, vol. 10, pp. 645–647, 1998.

[36] K. Vahala, L.C. Chiu, S. Margalit, and A. Yariv, "On the linewidth enhancement factor in semiconductor lasers," *Appl. Phys. Lett.*, vol. 42, pp. 631–633, 1983.

[37] M. Osinski and J. Buus, "Linewidth broadening factor in semiconductor lasers - an overview," *IEEE J. Quantum Electron.*, vol. QE-23, pp. 9–28, 1987.

[38] P. Vankwidkelberge, F. Buytaert, A. Franchois, R. Baets, P. Kuinersma, and C. Fredriksz, "Analysis of the carrier-induced FM response of DFB lasers: Theoretical and experimental case studies," *IEEE J. Quantum Electron.*, vol. 25, pp. 2239–2254, 1989.

[39] G. Morthier and P. Vankwikelberge, *Handbook of Distributed Feedback Laser*

Diodes, Artech House, Inc., 1997.

[40] R. Schatz, "Dynamics of spatial hole burning effects in DFB lasers," *IEEE J. Quantum Electron.*, vol. 31, pp. 1981–1993, 1995.

[41] G. Arfken, *Mathematical Methods for Physicists*, Harcourt, 4th edition, 1995, Ch. 11.

[42] L.A. Coldren and S.W. Corzine, *Diode Lasers and Photonic Integrated Circuits*, John Wiley & Sons, 1995.

[43] K. Petermann, *Laser Diode Modulation and Noise*, vol. p.85, Kluwer Academic Publishers, Boston, MA, 1988.

[44] S.A. Anson, J.T. Olesberg, M.E. Flatte, and T.C. Hansenberg, "Differential gain, differential index and linewidth enhancement factor for a 4 μm superlattice laser active layer," *J. Appl. Phys.*, vol. 86, pp. 713–718, 1999.

[45] G.H.B. Thompson, *Physics of Semiconductor Laser Devices*, John Wiley & Sons, 1980 p.536.

[46] M.R. Phillips, T.E.Darcie, and E.J.Flynn, "Experimental measure of dynamic spatial-hole burning in DFB lasers," *IEEE Photon. Technol. Lett.*, vol. 11, pp. 1201–1203, 1992.

[47] D.T. Cassidy, "Technique for measurement of the gain spectra of semiconductor diode lasers," *J. Appl. Phys.*, vol. 56, pp. 3096–3099, 1984.

[48] F. Devaux, Y. Sorel, and J.F. Kerdiles, "Simple measurement of fiber dispersion and of chirp parameter of intensity modulated light emitter," *IEEE J. Lightwave Tech.*, vol. 11, pp. 1937–1940, 1993.